AFIT/GE/ENG/04-02

FORWARD LOOKING RADAR: INTERFERENCE MODELLING, CHARACTERIZATION, AND SUPPRESSION

THESIS
James T. Caldwell
Second Lieutenant, USAF

AFIT/GE/ENG/04-02

DEPARTMENT OF THE AIR FORCE

AIR UNIVERSITY

AIR FORCE INSTITUTE OF TECHNOLOGY

Wright-Patterson Air Force Base, Ohio

AFIT/GE/ENG/04-02

FORWARD LOOKING RADAR: INTERFERENCE MODELLING, CHARACTERIZATION, AND SUPPRESSION

THESIS

Presented to the Faculty
Department of Electrical and Computer Engineering
Graduate School of Engineering and Management
Air Force Institute of Technology
Air University
Air Education and Training Command
In Partial Fulfillment of the Requirements for the
Degree of Master of Science in Electrical Engineering

James T. Caldwell, B.S.E.E.
Second Lieutenant, USAF

March, 2004

AFIT/GE/ENG/04-02

FORWARD LOOKING RADAR: INTERFERENCE MODELLING, CHARACTERIZATION, AND SUPPRESSION

THESIS

James T. Caldwell, B.S.E.E.
Second Lieutenant, USAF

Approved:

/signed/ 2/27/04
Maj Todd B. Hale, Ph.D. Date
Thesis Advisor

/signed/ 2/27/04
Maj Matthew E. Goda, Ph.D. Date
Committee Member

/signed/ 2/25/04
Dr. Michael A. Temple Date
Committee Member

Acknowledgements

First and foremost, I owe a large debt of gratitude to my parents who always emphasized the importance of education. Additionally, I would like to thank my advisor, Maj Todd Hale, for always taking the time to answer my questions and whose technical knowledge was invaluable.

James T. Caldwell

Table of Contents

Page

List of Figures

List of Tables

Table Page

List of Symbols

Symbol		Page
T_r	Pulse Repetition Interval	6
$\bar{\omega}_t$	Normalized Doppler	6
f_t	Target Doppler shift	6
f_r	Pulse Repetition Frequency	6
P_{fa}	False alarm probability	6
P	Number of elevation elements	7
N	Number of azimuth elements	7
d_x	Azimuth inter-element spacing	7
d_z	Elevation inter-element spacing	7
$\hat{\mathbf{k}}$	Unit vector	7
ϕ	Phi	7
θ	Theta	7
a_t	Transmitted pulse amplitude	9
$u(t)$	Pulse train envelope function	9
ω_o	Carrier frequency	9
ψ	Random phase	9
T_p	Pulse width	9
M	Number of pulses	9
τ_{np}	Round trip time delay	10
v_r	Relative velocity	10
λ_o	Radar wavelength	10
a_r	Received pulse amplitude	10
α_t	Complex received amplitude	11
ϑ_x	X-axis spatial frequency	11
ϑ_z	Z-axis spatial frequency	11
$\boldsymbol{\chi}_t$	Space-time snapshot	11
$\mathbf{v}_t$	Steering vector	11
σ^2	Noise Power	13
ξ_j	Jammer to noise ratio	14
ξ_{ik}	Clutter to noise ratio	15
N_c	Number of clutter patches	15
N_r	Number of ambiguous range rings	15
$\mathbf{R}$	Covariance matrix	16
$\hat{\mathbf{R}}$	Covariance matrix estimate	19

Symbol		Page
$\mathbf{T}$	Transformation matrix	20
$\mathbf{a}$	azimuth steering vector	31
$\mathbf{b}$	temporal steering vector	31
$\mathbf{e}$	elevation steering vector	31
B_c	Normalized clutter bandwidth	39

List of Abbreviations

Abbreviation		Page
STAP	Space-Time Adaptive Processing	1
SINR	Signal-to-Interference-plus-Noise Ratio	1
MF	Matched Filter	2
JDL	Joint Domain Localized	2
PAMF	Parametric Adaptive Matched Filter	2
FTS	Factored Time Space	2
SM	Signal Match	3
AFRL	Air Force Research Laboratory	4
SNR	Radio Frequency Sensor Technology Division	4
CW	Continuous Wave	5
PRF	Pulse Repetition Frequency	6
PRI	Pulse Repetition Interval	6
CPI	Coherent Processing Interval	9
RCS	Radar Cross Section	10
PSD	Power Spectral Density	13
JNR	Jammer to Noise Ratio	14
CNR	Clutter to Noise Ratio	15
ICM	Internal Clutter Motion	15
SNR	Signal to Noise Ratio	17
ML	Maximum Likelihood	17
DOF	Degrees of Freedom	18
AR	Auto-Regressive	18
iid	Independent Identically Distributed	19
LPR	Localized Processing Region	20
SAP	Spatially Adaptive Processing	21
TFACF	Time-Frequency Auto-Correlation Function	30
MTI	Moving Target Indicator	53
DFT	Discrete Fourier Transform	62

AFIT/GE/ENG/04-02

Abstract

This research characterizes forward looking radar performance while noting differences with traditionally examined sidelooking radar. The target detection problem for forward looking radar is extremely difficult due to the severe, heterogeneous, and range dependent ground clutter. Consequently, forward looking radar detection represents an important but overlooked topic because of the increased difficulty compared to sidelooking radar. This void must be filled since most fighter aircraft use forward looking radar, making this topic intensely interesting to the Air Force.

After characterizing forward looking radar performance, basic radar concepts along with advanced adaptive interference suppression techniques improve the output Signal-to-Interference-plus-Noise Ratio (SINR) and target detection rates using fixed false alarm for linear arrays. However, target detection probabilities and output SINR do not improve enough. Although the methods considered are adaptive in azimuth and Doppler, effective range ambiguous clutter mitigation requires elevation adaptivity, a feature not offered by linear arrays.

The research continues by examining planar arrays. Elevation adaptivity combined with azimuth and Doppler adaptivity allows suppressing range ambiguous clutter and significantly increasing output SINR, detection probability, and maximum detection range. Specifically, three-dimensional Space-Time Adaptive Processing (3D STAP) techniques with adaptivity in elevation, azimuth, and Doppler achieve detection probability improvements of over 10 dB in required input SINR compared to two-dimensional (2D) STAP processing. Additionally, 3D STAP improves detection probability versus input SINR curves over 30 dB when compared to 2D conventional processing techniques.

As a result, forward looking radars using 3D STAP have the capacity to detect targets that conventional processing might miss.

FORWARD LOOKING RADAR: INTERFERENCE MODELLING, CHARACTERIZATION, AND SUPPRESSION

I. Introduction

Airborne radar systems are required to detect increasingly smaller targets obscured by interference. Conventional Doppler filtering separates the target from the interference in the frequency domain. However, complex interference environments mitigate the advantages associated with Doppler filtering because some targets residing near mainbeam clutter remain difficult to detect. To date, only adaptive interference suppression techniques offer the improved detection required for these smaller, obscured targets in clutter limited environments. One form of adaptive interference suppression processing is called Space-Time Adaptive Processing (STAP). Such processing methods adaptively process radar data both spatially (with respect to the antenna array) and temporally (with respect to Doppler filtering). STAP provides improved detection by maximizing output Signal-to-Interference-plus-Noise Ratio (SINR) .

1.1 Purpose

This research fills a void in the adaptive interference suppression literature base since most STAP research predominately focuses on the sidelooking array case [1]. Although typical surveillance radar platforms do use the sidelooking array configuration, adaptive interference suppression method research is now transitioning to fighter aircraft and other platforms. These platforms typically use a forward looking array and exhibit a much stronger interference environment due to aircraft dynamics.

This thesis characterizes the forward looking array, discusses forward looking array effects on radar performance, and applies basic radar concepts along with advanced STAP techniques to improve output SINR and target detection. Forward looking and sidelooking array cases are examined and differences noted.

1.2 Organization

Chapter II provides a literature review describing the sidelooking array data model. This model is based on Ward's physical model for linear arrays [2] with extensions to planar arrays by Hale [3] and decorrelation effects by Klemm [1] and Jaffer [4]. Also, the literature review provides a basic STAP background. The sidelooking array data model is important because it serves as the framework for the forward looking data model.

Chapter III develops the forward looking data model. This data model is developed mathematically using a planar array with the aircraft's velocity along the antenna array boresight and using a 90° crab angle on the sidelooking data model. A crab angle occurs when the real velocity vector differs from the aircraft's longitudinal axis. Therefore, a 90° crab angle on the sidelooking array case alters the velocity vector such that it lies along antenna array boresight, i.e., it simulates a forward looking array. The equivalence of these two forward looking array implementations is shown.

Chapter IV compares the forward looking array to the sidelooking array, illustrating a more severe interference environment with more clutter heterogeneities and multiple clutter ridges due to range ambiguous clutter. Also, decorrelation effects have a more pronounced effect on the forward looking array case as shown in output SINR plots.

Chapter V applies STAP to the forward looking case, mitigating the increased interference environment. Several different STAP technique performance results are examined including the Matched Filter (MF), Joint Domain Localized (JDL), Parametric Adaptive Matched Filter (PAMF) and Factored Time-Space (FTS). Also, non-adaptive beamforming and conventional Doppler filtering is used and referred to as Signal Match (SM). The SM processing technique is a useful comparison because it shows radar system performance without STAP, illustrating performance improvements due to adaptivity. Since maximizing output SINR also maximizes detection probability performance, output SINR analysis is used to evaluate performance [5]. Following the output SINR analysis, antenna beam patterns are shown for the forward looking array case. Antenna beam patterns allow observation of null placement with comparison to interference power spectral density surfaces. The idea is for the antenna beam pattern to null the clutter and the jammer while having a peak response in the desired look direction. Lastly, Monte Carlo analysis is used to predict detection probability performance.

Additionally, changing the Pulse Repetition Frequency (PRF) is presented as a path to changing the target location in the Doppler space. Even with the improvements in SINR, three-dimensional (3D) STAP is needed to improve target detection around the clutter ridges for the forward looking array case since the forward looking interference environment is so severe.

Chapter VI examines 3D STAP processing. The elevation adaptivity addition allows multiple-time around clutter cancellation. Hence, foldover in the forward looking array case no longer obscures targets. Analysis focuses on how 3D STAP processing alleviates the decorrelation effects plaguing forward looking radar returns and improves SINR Loss, detection probability performance, and maximum detection range.

1.3 Notation

Table 1.1 describes the notation used throughout this thesis. The only ambiguity that exists in this notation is whether a quantity is estimated or in fact a unit vector. Surrounding text clarifies whether quantities are estimated or whether they are unit vectors when they are introduced.

Table 1.1: Thesis notation.

Example	Definition
$\mathbf{x}$	Vectors
$\mathbf{X}$	Matrices
x	Scalars
$\hat{k}$	Estimated parameter or unit vector
x^H	Hermitian Transpose
x^T	Transpose
x^*	Complex Conjugation
$\mathbf{X}_{n,m}$	n^{th} row and m^{th} column
$\mathbf{x}_n$	n^{th} vector element
ϕ_t	Describes "t" is for target
$\varepsilon[\cdot]$	Expected value

1.4 Sponsorship

The Air Force Research Laboratory (AFRL) is very interested in applying STAP to improve target detection in airborne radars using forward looking arrays. This interest occurs because most fighters use forward looking arrays.

The AFRL Radio Frequency Sensor Technology Division (SNR) conducts research and development programs demonstrating radar target detection and adaptive radar processing. These programs meet the Air Force's needs in the targeting, attack, and weapon delivery areas for vehicles. This thesis supports AFRL/SNR's mission of increased target detection and adaptive radar processing for forward looking radar systems.

II. Sidelooking Radar Modelling and Adaptive Interference Suppression

This chapter focuses on modelling sidelooking array radar data and interference suppression methods. This model then serves as the foundation for modelling forward looking array data in Chapter III.

Careful consideration should be used by the reader when reading Chapter II. Although, forward looking arrays are the focus of this thesis, sidelooking arrays form the bulk of available literature. Understanding sidelooking arrays is critical to understanding the forward looking array model. The sidelooking array model presented here is based on the physical model by Ward [2] with extension to planar arrays by Hale [3] and added decorrelation effects by Klemm [1] and Jaffer [4]. These three facets are presented in a cohesive framework within this document.

The logical progression when describing Space-Time Adaptive Processing (STAP) applied to sidelooking arrays includes a quick airborne radar problem overview, data model description, a basic background on STAP, and fundamental STAP implementation issues. Section 2.1 gives the airborne radar overview. Section 2.2 describes the sidelooking array data model. Section 2.3 provides the STAP background. Finally, Section 2.4 goes over fundamental STAP implementation issues and Section 2.5 reviews another STAP approach using parametric modelling.

2.1 Airborne Radar Problem Overview

Airborne radars must compensate for noise and interference typically several orders of magnitude larger than target echoes [6]. The traditional way of dealing with this problem is to take advantage of the Doppler effect, a frequency shift due to a difference in relative velocity between the airborne radar and its target. Continuous Wave (CW) radars constantly transmit a sinusoidal waveform and obtain a target velocity estimate from the Doppler shift. CW radars cannot differentiate the time it takes for a particular wave to travel to the target and back to the radar because all waves are identical resulting in no range information. As a result, radars transmit pulsed waveforms in order to gain both range and velocity information about potential targets.

Pulsed Doppler radars use a medium-to-high Pulse Repetition Frequency (PRF) so there are not many Doppler frequency ambiguities but as a result there are some range ambiguities. The Pulse Repetition Interval (PRI) defines the time between pulses and is denoted as T_r. The PRI and PRF are inverses of each other and set the number of range and Doppler ambiguities. Normalized Doppler, $\bar{\omega}_t$, is defined as the Doppler shift, f_t, normalized by the PRF, f_r,

$$\bar{\omega}_t = \frac{f_t}{f_r}. \tag{2.1}$$

Any normalized Doppler value greater than 0.5 or less than -0.5 is ambiguous. Therefore, any value lying outside this range is easily discernable as Doppler ambiguous.

Radars receive these pulses at each antenna element and process them to determine whether a target is present or not. All STAP approaches combine weighted sums of the pulses from every antenna element to form a scalar quantity. This scalar is then threshold detected to determine if a target is present. Radar target detection is a form of Neyman-Pearson testing [7] where the desired false alarm probability (P_{fa}) determines the threshold. The weights can be fully adaptive where the pulses from every antenna element are utilized adaptively or partially adaptive where only a set number of weights are adaptive.

The clutter returns experience the Doppler shift for airborne radars and consequently radars that use traditional Signal Match (SM) processing may not be able to separate slow moving targets from mainbeam clutter.

$\boxed{!}$ Signal Match (SM) processing refers to conventional filtering techniques using non-adaptive beamforming and Doppler filtering.

For this reason, adaptive processing is used to place nulls along the clutter ridge to increase the Signal-to-Interference-plus-Noise Ratio (SINR) and detection probability. For sidelooking arrays, the clutter ridge is shown to be linear with sine of azimuth versus Doppler frequency verifying STAP is required because STAP is adaptive both spatially and temporally.

2.2 Data Model for Side Looking Arrays

Traditionally, most STAP research focuses on sidelooking arrays for airborne pulsed radars [1]. Neglecting crab angle and yaw, aircraft with sidelooking arrays move with a velocity along the positive x-axis. The data model presented below closely follows the accepted sidelooking model [2, 3].

The planar radar antenna array is composed of P stacked linear arrays with N equidistant elements. These linear arrays extend along the x-axis and P of them are placed along the z-axis. These elements are equidistantly separated in azimuth and elevation with distances d_x and d_z, respectively. Figure 2.1 shows the planar array model used in this thesis.

A unit vector pointing to an arbitrary point is expressed in Cartesian coordinates as

$$\hat{\mathbf{k}}(\phi, \theta) = \cos(\theta)\sin(\phi)\hat{\mathbf{x}} + \cos(\theta)\cos(\phi)\hat{\mathbf{y}} + \sin(\theta)\hat{\mathbf{z}}, \tag{2.2}$$

where $\hat{\mathbf{k}}$ is the unit vector, ϕ is the azimuth angle, θ is the elevation angle, and $\hat{\mathbf{x}}$, $\hat{\mathbf{y}}$, and $\hat{\mathbf{z}}$ are the cartesian unit vectors. The radar coordinate system is similar to the spherical coordinate system but true azimuth and true elevation are used. Therefore, θ is negative when pointing towards the ground because it is below radar boresight. Additionally, ϕ is zero at radar boresight (along the positive y-axis) and is positive as ϕ moves towards the positive x-axis from the positive y-axis. The position vector

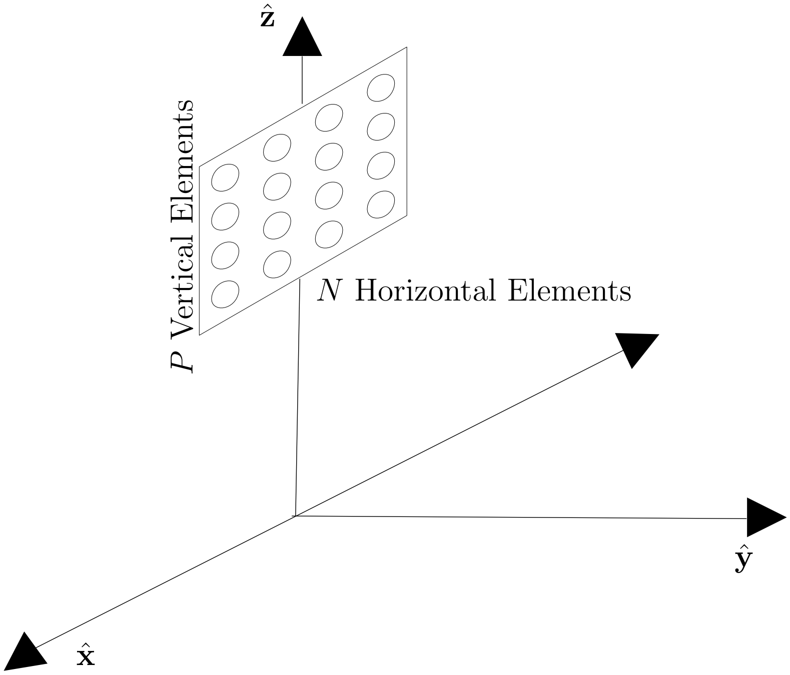

Figure 2.1: Planar array model with P vertical elements spaced d_z apart and N horizontal elements spaced d_x apart.

$\mathbf{d}_{np}$ describes the position of element np in the antenna array and is given as

$$\mathbf{d}_{np} = nd_x\hat{\mathbf{x}} + pd_z\hat{\mathbf{z}}, \tag{2.3}$$

where $n = 0, 1, ..., N - 1$ and $p = 0, 1, ..., P - 1$.

$\boxed{!}$ When $P = 1$, the planar array reduces to the linear array that is common in most STAP publications.

2.2.1 Radar Waveform. Since the radar system and geometry have been described, the discussion changes to the transmit and receive radar waveform. Ultimately, the radar returns are received, frequency down converted, matched filtered, and digitized before adaptive processing as shown in Fig. 2.2. Using complex expo-

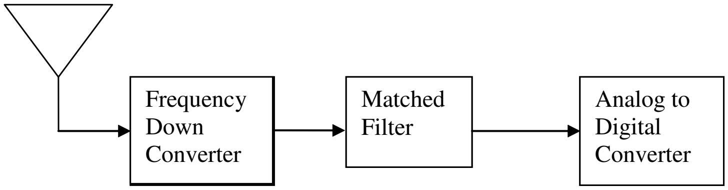

Figure 2.2: Radar block diagram for data collection.

nential notation, the transmitted radar waveform is modelled as

$$s(t) = a_t u(t) e^{j(\omega_o t + \psi)}, \tag{2.4}$$

where a_t is an amplitude, $u(t)$ is defined in Eqn. (2.5), ω_o is the radian carrier frequency, and ψ is a random phase [3]. The pulsed structure is defined by the pulse width T_p and PRI [6]. M pulses with width T_p sum together to yield the envelope function

$$u(t) = \sum_{m=0}^{M-1} u_p(t - mT_r), \tag{2.5}$$

where the individual pulses, $u_p(t)$, are shifted by integer multiples of the PRI, T_r. The basic pulse used in radar is

$$\begin{aligned} u_p(t) &= 1 \quad 0 \leq t \leq T_p \\ &= 0 \quad \text{otherwise.} \end{aligned} \tag{2.6}$$

The Coherent Processing Interval (CPI) is defined by the finite coherent summation of M pulses. The transmitted radar pulse train multiplied by the sinusoidal carrier frequency is shown in Fig. 2.3. For Fig. 2.3, the PRI is 3 seconds and the pulse width is 1 second.

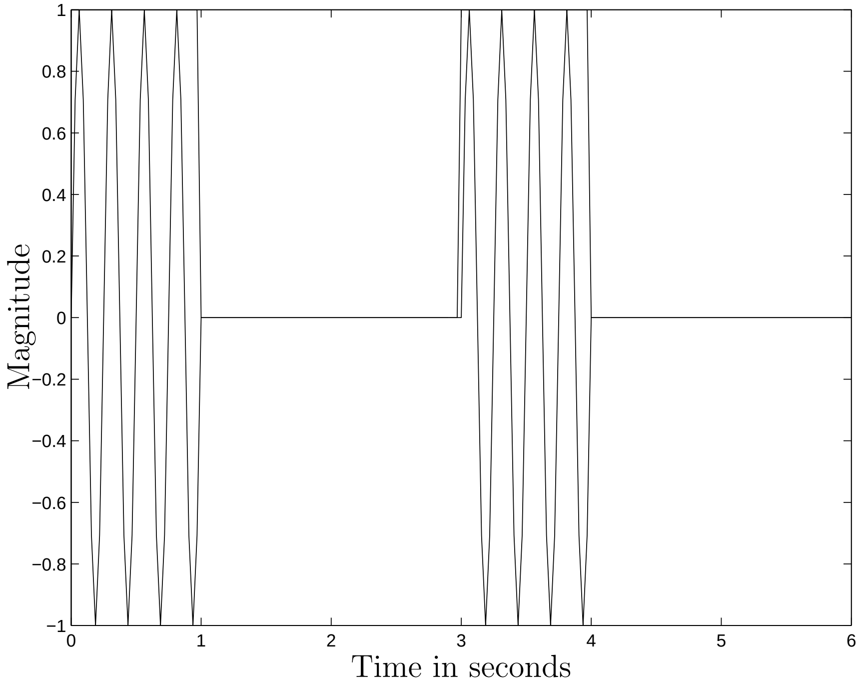

Figure 2.3: Transmitted radar pulse train modulating sinusoidal carrier.

Next, each antenna element (channel) receives the radar waveform with a time delay, τ_{np}, and Doppler shift (assumed to be equal at every antenna element) due to the relative motion between the aircraft and the target. The Doppler frequency shift is defined as

$$f_t = \frac{2v_r}{\lambda_o}, \tag{2.7}$$

where v_r is the relative velocity between the aircraft and the target and λ_o is the radar's transmit wavelength [8]. At element np, the received waveform is represented as

$$s_{np}(t) = a_r u(t - \tau_{np}) e^{j2\pi f_o (t-\tau_{np})} e^{j2\pi f_t (t-\tau_{np})} e^{j\psi}, \tag{2.8}$$

where a_r is the received amplitude. The parameter a_r accommodates range attenuation and Radar Cross Section (RCS) effects and is calculated using the radar range equation discussed in [6]. After removing the carrier frequency and match filtering on a pulse-by-pulse basis, the received signal at a particular np^{th} element, for the

m^{th} pulse, and from a particular range cell is

$$\chi_{mnp} = \alpha_t e^{j2\pi(n\vartheta_x + p\vartheta_z)} e^{j2\pi m\bar{\omega}_t}, \tag{2.9}$$

where $a_r e^{j\psi}$ is replaced by the complex quantity α_t. ϑ_x and ϑ_z represent spatial frequencies defined in Section 3.1.2. The return in Eqn. (2.9) represents the return from a single point scatterer.

2.2.2 Data Format. After the radar signal has been received, down converted, and match filtered, the data needs to be put into some mathematical format suitable for customary linear algebra operations. This formatting is accomplished using the Kronecker product [9]. The three-dimensional (3D) space-time snapshot $\boldsymbol{\chi}_t$ for a given range cell is

$$\boldsymbol{\chi}_t = \alpha_t \mathbf{e}(\vartheta_z) \otimes \mathbf{b}(\bar{\omega}_t) \otimes \mathbf{a}(\vartheta_x), \tag{2.10}$$

where $\otimes$ is the Kronecker product. $\mathbf{e}(\vartheta_z)$, $\mathbf{b}(\bar{\omega}_t)$, and $\mathbf{a}(\vartheta_x)$ represent the steering vectors defined in Section 3.1.4.

The space-time snapshot represents MNP samples for each range cell. There are L range cells, each of size $\frac{cT_p}{2}$ meters across, representing successive range gates up to the unambiguous range given in Eqn. (3.38). When $P = 1$, the data is conceptually visualized using the datacube as seen in Fig. 2.4. For planar arrays when P is greater than one, the data is visualized using a hypercube, a difficult concept to picture.

The 3D steering vector $\mathbf{v}_t$ is defined as

$$\mathbf{v}_t = \mathbf{e}(\vartheta_z) \otimes \mathbf{b}(\bar{\omega}_t) \otimes \mathbf{a}(\vartheta_x). \tag{2.11}$$

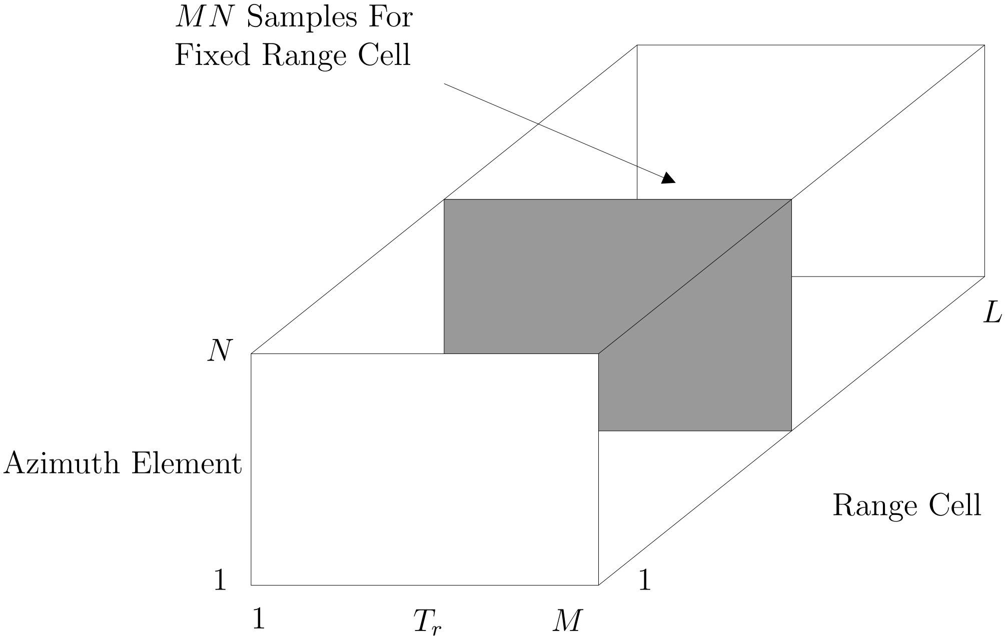

Figure 2.4: Radar datacube for linear arrays when $P = 1$. Other values of P require visualization of a 4D hypercube.

The space-time steering vector physically represents the phase changes on every channel and pulse return for a single point scatterer at some location in elevation, azimuth, and normalized Doppler referenced to one of the elements and pulses within the CPI [10]. Using the steering vector, the space-time snapshot can be represented as

$$\boldsymbol{\chi}_t = \alpha_t \mathbf{v}_t. \tag{2.12}$$

The space-time snapshot physically represents the return from a single point scatterer.

In real radar systems, the return due to the target has to compete with undesirable returns. Hence, the received data is represented as

$$\boldsymbol{\chi} = \boldsymbol{\chi}_t + \boldsymbol{\chi}_u, \tag{2.13}$$

where the undesirable returns are composed of thermal noise, barrage noise jamming, and clutter. This model uses a single point scatterer for the target return and therefore adds in thermal noise, jamming, and clutter to the data.

2.2.3 Thermal Noise Model. Only white Gaussian thermal noise is assumed present in the data. This noise is internally generated by the receivers, and given every element has its own receiver, the noise is mutually independent for every element. The correlation matrix for the noise component is defined as

$$\mathbf{R}_n = \varepsilon[\boldsymbol{\chi}_n \boldsymbol{\chi}_n^H]. \tag{2.14}$$

The correlation matrix for independent random processes is the identity matrix [11]. The thermal noise is assumed to be zero mean, since there is no direct current component within the return. For zero mean random processes, the covariance matrix is equal to the correlation matrix. Therefore, the noise covariance matrix is equal to

$$\mathbf{R}_n = \sigma^2 \mathbf{I}_{MNP}, \tag{2.15}$$

where σ^2 is the noise power and $\mathbf{I}_{MNP}$ is an identity matrix with dimensions $MNP \times MNP$. The noise power is equal to N_oB, where N_o is the noise Power Spectral Density (PSD) and B is the radar bandwidth. It is important to note the thermal noise guarantees the covariance matrix is non-singular.

2.2.4 Jammer Model. This thesis only takes into account noise jamming. Noise jammer signals are uncorrelated temporally but correlated spatially. The spatial correlation property creates a spatial relationship between the returns across the array elements. Similarly, the temporally uncorrelated property destroys any Doppler information as the returns from pulse-to-pulse are uncorrelated. Since there is no direct current component in the jammer returns, the jammer covariance matrix is equivalent to the jammer correlation matrix. Using the properties of the Kronecker

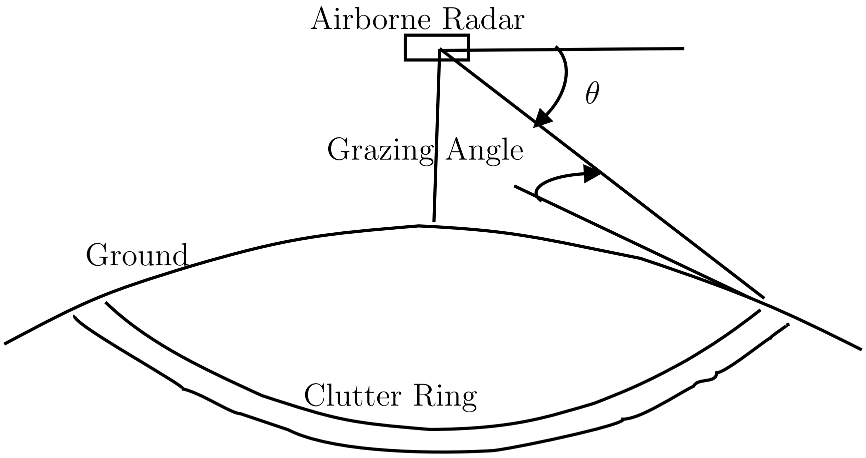

Figure 2.5: Clutter ring for an airborne radar.

product and following the process in [3], the jammer covariance matrix is

$$\mathbf{R}_j = \sigma^2 \xi_j \mathbf{e}(\vartheta_z)\mathbf{e}^H(\vartheta_z) \otimes \mathbf{I}_M \otimes \mathbf{a}(\vartheta_x)\mathbf{a}^H(\vartheta_x), \tag{2.16}$$

where ξ_j is the Jammer to Noise Ratio (JNR).

2.2.5 Clutter Model. The airborne clutter model established by [3] takes into account ambiguous clutter returns and planar arrays. This model is an extension to the physical model developed by [2] with added decorrelation effects by [1] and [4]. Since ground returns are typically much larger than sky clutter, any sky clutter returns have been ignored. A 4/3 effective radius is used to model the earth as a sphere.

Due to range ambiguities associated with pulsed radar signals, the radar receives clutter returns for the same range cell at multiples of the unambiguous range up to the horizon range. Each range ring consists of clutter patches with a certain RCS and grazing angle as discussed in [6]. Figure 2.5 shows the clutter ring for an airborne radar.

The clutter Doppler frequency f_c at any patch is

$$f_c(\theta_i, \phi_k) = \frac{2\hat{\mathbf{k}}(\theta_i, \phi_k) \bullet \mathbf{v}_a}{\lambda_o}, \tag{2.17}$$

where $\bullet$ is the dot product. Recalling that for sidelooking radar the velocity vector is totally along the x-axis (assuming zero crab angle), the clutter Doppler frequency becomes

$$f_c^{SL}(\theta_i, \phi_k) = \frac{2v_a \cos(\theta_i)\sin(\phi_k)}{\lambda_o}. \tag{2.18}$$

Notice the mainbeam clutter in the sidelooking array case is range independent, because the clutter ridge always passes through 0 Hz for the main beam (0° azimuth) regardless of range. The clutter returns are again zero mean so that the covariance matrix is equal to the correlation matrix. The clutter covariance matrix is then written as

$$\mathbf{R}_c = \sigma^2 \sum_{i=1}^{N_c} \sum_{k=1}^{N_r} \xi_{ik} \mathbf{e}(\vartheta_z)\mathbf{e}^H(\vartheta_z) \otimes \mathbf{b}(\bar{\omega}_{ik})\mathbf{b}^H(\bar{\omega}_{ik}) \otimes \mathbf{a}(\vartheta_x)\mathbf{a}^H(\vartheta_x), \tag{2.19}$$

where ξ_{ik} is the Clutter to Noise Ratio (CNR), N_c is the number of clutter patches, and N_r is the number of ambiguous range rings.

$\boxed{!}$ Important: for ranges less than the altitude, only ambiguous clutter returns are present.

2.2.5.1 Decorrelation Effects. The data model incorporates real world effects using decorrelation parameters. The decorrelation effects comprise Internal Clutter Motion (ICM) [1,4] and System Bandwidth [1]. The decorrelation effects are applied to the clutter covariance matrix using statistical decorrelation coefficients from [1] to incorporate ICM and System Bandwidth. ICM represents clutter motion within a patch, above and beyond the relative velocity from platform motion. This effect commonly occurs when foliage moves as a result of wind. Real radars must compensate for this increased clutter bandwidth. System Bandwidth accounts for spatial decorrelation across the array resulting from different propagation times on an element-by-element basis, when the clutter receive signal arrives at angles other than boresight. Standard array theory aligns receive signals on an element-by-element basis using phase delays. Therefore, the actual pulse envelope does not completely align at every element and a loss is incurred. This loss is accounted for using the System Bandwidth decorrelation effect. Both decorrelation effects result in increased clutter covariance matrix rank. Section 3.4 shows the actual implementation of the decorrelation effects.

2.2.6 Total Interference plus Noise Covariance Matrix. The next step consolidates the different components into the total covariance matrix. Typically, radar returns are assumed to be one of two hypotheses. The H_1 hypothesis is

$$\boldsymbol{\chi} = \boldsymbol{\chi}_t + \boldsymbol{\chi}_c + \boldsymbol{\chi}_n + \boldsymbol{\chi}_j, \tag{2.20}$$

meaning the target is present. The H_0 hypothesis occurs when no target is present,

$$\boldsymbol{\chi} = \boldsymbol{\chi}_c + \boldsymbol{\chi}_n + \boldsymbol{\chi}_j. \tag{2.21}$$

The total covariance matrix is computed under the H_0 hypothesis

$$\mathbf{R} = \varepsilon[\boldsymbol{\chi}\boldsymbol{\chi}^H] = \mathbf{R}_c + \mathbf{R}_j + \mathbf{R}_n, \tag{2.22}$$

where $\mathbf{R}$ is the interference plus noise covariance matrix and assuming that the noise, jammer, and clutter returns are all mutually uncorrelated. The covariance matrix has dimensions $MNP \times MNP$.

> $\boxed{!}$ The ambiguous clutter returns that this model incorporate are very important but unfortunately usually ignored in traditional STAP research. Elevation adaptivity can null out ambiguous clutter range rings [3]. Regular linear arrays lack elevation adaptivity and thus cannot null out ambiguous clutter as well as planar arrays.

2.3 Background on STAP

Clutter limited, versus thermal noise limited, target detection remains a difficult task for any airborne radar [6]. Conventional Doppler filtering offers significant improvement by placing the target and interference in a domain where they can be separated based on Doppler shift. However, clutter limited interference environments mitigate the advantages associated with Doppler filtering techniques. In particular, slow moving targets residing near mainbeam clutter remain difficult to detect.

Adaptive interference suppression research serves to solve this complex clutter limited airborne radar problem. Typically, STAP refers to two-dimensional (2D) spatial and temporal adaptive processing methods. The first publication suggesting such an approach focused on a fully adaptive method and illustrated optimality by maximizing the output Signal-to-Interference-plus-Noise Ratio (SINR) using known interference statistics [12]. This approach became commonly known as the Matched Filter (MF), not to be confused with conventional matched filtering techniques such as those discussed in [6]. Such conventional (nonadaptive) matched filtering techniques maximize output Signal-to-Noise Ratio (SNR) given white Gaussian thermal noise as the interference source.

> ! The reader should take care to notice there is a fundamental difference between the MF and a matched filter despite the similarity of the nomenclature. The MF is the optimum space-time processing filter used in STAP whereas a matched filter is a generic filter that seeks to maximize a received SNR before signal processing.

Unfortunately, interference statistics are not known *a priori* and must be estimated from available data if used in any practical radar system. This realization resulted in the Adaptive Matched Filter (AMF) [5], where known interference statistics are replaced by a Maximum Likelihood (ML) estimate formulated from received airborne radar data. The AMF brought about new problems since fully adaptive methods such as the AMF require large amounts of radar data (possibly more than is available) when calculating the interference estimate. Due to sample support limitations and large computational load, researchers began working on partially adaptive methods (reduced dimension problems).

Partially adaptive STAP algorithms constrain the Degrees of Freedom (DOF) available for interference suppression. Such a constraint clearly fails to compete with fully adaptive methods, but is actually implementable and able to estimate interference statistics. A wide variety of partially adaptive methods exist. The most simple partially adaptive algorithm considered is a factored approach, Factored Time-Space (FTS) [2].

Two other partially adaptive interference suppression methods offer interesting approaches. The first reduces dimensionality, and subsequently computational load and sample support requirements, by first projecting the data into a domain where the target is localized to a single bin or cell. In the ideal radar context, this domain is angle-Doppler. A small localized processing region is formed around this bin where localized adaptivity is implemented and target detection achieved. This method is commonly known as Joint Domain Localized (JDL) [13].

The second method is the Parametric Adaptive Matched Filter (PAMF) [14]. The PAMF offers a truly revolutionary approach to the adaptive interference suppression problem. All previous approaches relied on interference statistics estimates in the form of covariance matrices. The PAMF approach applies an Auto-Regressive (AR) model and approaches performance parallelling fully adaptive methods with extremely small sample support. The primary weakness associated with the PAMF approach is appropriate AR model selection.

2.4 Implementation of STAP

In general, the output of any radar filter is threshold detected. The filter output is in general,

$$y = \mathbf{w}^H \boldsymbol{\chi}, \tag{2.23}$$

where y is threshold detected and $\mathbf{w}$ is the weight vector. The optimum space-time filter, also known as the (MF), weight vector equals

$$\mathbf{w}_o = \mathbf{R}^{-1}\mathbf{v}_t. \tag{2.24}$$

However, the interference plus noise covariance matrix is never known *a priori* but the MF serves as a benchmark for comparison. Therefore, STAP seeks to maximize the SINR adaptively and reach as close as possible to the MF's optimal performance.

As discussed in Section 2.3 the AMF estimates the covariance matrix and has the following weight vector,

$$\mathbf{w}_{\text{amf}} = \hat{\mathbf{R}}^{-1}\mathbf{v}_t, \tag{2.25}$$

where $\hat{\mathbf{R}}$ is the ML covariance matrix estimate. Ensuring the covariance matrix estimate is non-singular requires at least MNP Independent Identically Distributed (iid) range cells for sample support. The sample support needs to be iid so the statistics of the covariance matrix can be accurately estimated. The covariance matrix is estimated using the ML estimate as

$$\hat{\mathbf{R}} = \frac{1}{K}\sum_{k=1}^{K} \boldsymbol{\chi}_k \boldsymbol{\chi}_k^H, \tag{2.26}$$

where K is equal to the number of sample support used and $\boldsymbol{\chi}_k$ is the incoming data vector from the k^{th} secondary support range cell. Also, the estimation of the covariance matrix impacts AMF performance. Reed's Rule states for the output SINR to be within 3 dB of the optimum (known covariance) SINR on average, twice the number of DOF sample support is required for estimating the covariance matrix [15, 16]. Therefore, AMF requires MNP iid samples to even work but needs $2MNP$ iid samples for performance to be within 3 dB of the MF's performance.

JDL is a partially adaptive STAP technique presented by Wang and Cai [13]. JDL offers a beamspace approach that is only adaptive within a Localized Processing

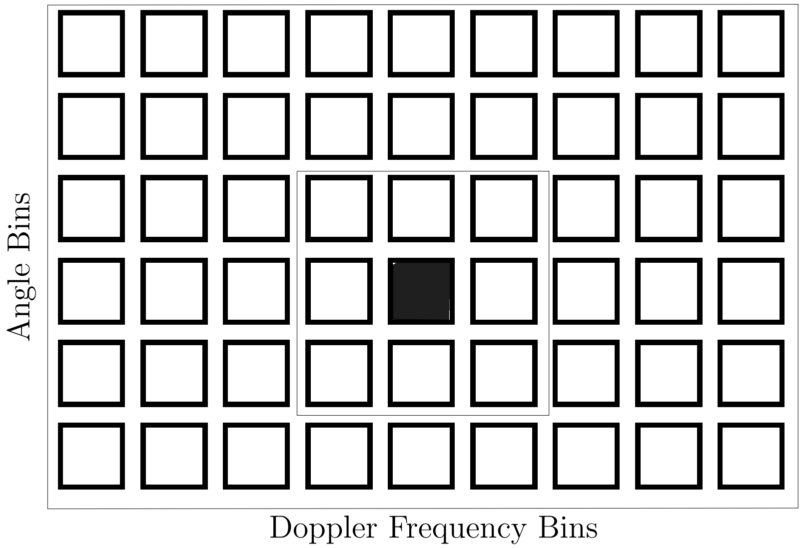

Figure 2.6: JDL Localized Processing Region (LPR) corresponding to a 3 × 3 LPR with the bin corresponding to the signal darkened.

Region (LPR). Beamspaces result from forming a beam to bins located at a certain frequency and angle. The received space-time data must first be transformed to the angle-Doppler domain. Additionally, for JDL to work under ideal conditions, the point target must be centered on a bin or the target will "bleed" to adjacent range cells. Figure 2.6 shows a 3 × 3 LPR with the darkened bin corresponding to the signal. JDL has the advantage of breaking a large problem into smaller problems while still achieving close to optimal results. Data is transformed from the element-time space to the angle-Doppler space by projecting into the LPR. The dimension reducing transformation matrix, $\mathbf{T}$, used to project into the LPR is

$$\mathbf{T} = \begin{bmatrix}\mathbf{e}(\theta_{-1}) & \mathbf{e}(\theta_0) & \mathbf{e}(\theta_1)\end{bmatrix} \otimes \begin{bmatrix}\mathbf{b}(\bar{\omega}_{-1}) & \mathbf{b}(\bar{\omega}_0) & \mathbf{b}(\bar{\omega}_1)\end{bmatrix} \otimes \begin{bmatrix}\mathbf{a}(\phi_{-1},\theta_0) & \mathbf{a}(\phi_0,\theta_0) & \mathbf{a}(\phi_1,\theta_0)\end{bmatrix}, \quad (2.27)$$

where $\bar{\omega}_{-1}$ represents a bin below the LPR center for Doppler, $\bar{\omega}_0$ represents the LPR center bin for Doppler, and the other parameters follow in the same manner. The transformation matrix above represents a 3x3x3 LPR where a generic LPR has size $\eta_e \times \eta_b \times \eta_a$. $\mathbf{T}$ has dimensions $MNP \times \eta_e\eta_b\eta_a$ where $\eta_e \leq$P, $\eta_b \leq$M, and $\eta_a \leq$N. The weight vector for JDL is [17]

$$\mathbf{w}_{\text{jdl}} = \mathbf{T}(\mathbf{T}^H\mathbf{R}\mathbf{T})^{-H}\mathbf{T}^H\mathbf{v}_t. \tag{2.28}$$

FTS is a post Doppler Spatially Adaptive Processing (SAP) techniques. FTS uses a factored approach that Doppler filters the data first and then adaptively beamforms the Doppler filtered data second [2]. FTS can be implemented by making an LPR region with only one Doppler bin. This removes the Doppler adaptivity present in JDL. The LPR region would consist of all the spatial bins.

The STAP algorithms discussed so far require a matrix inversion of either the estimated covariance matrix or $\mathbf{T}^H\hat{\mathbf{R}}\mathbf{T}$ as part of the algorithm. The operations required for matrix inversion are proportional to the size of the matrix cubed. This computational complexity poses a problem for fully adaptive STAP because MNP is usually a very large number in practice. The inversion of $\mathbf{T}^H\hat{\mathbf{R}}\mathbf{T}$ requires fewer operations due to the dimension reducing transformation matrix.

The computational complexity is not the only implementation issue for STAP. The covariance matrix or the dimension reduced covariance matrix must be inverted. This inversion requires a non-singular matrix (full rank). The dimension of the matrix to be inverted is the number of DOF that are adaptive. This means that the number of iid samples required for a full rank matrix is the number of DOF. For example, MNP sample data support is required for the AMF. However, partially adaptive STAP methods only require the number of DOF, usually much less than MNP. In reality, MNP iid sample support is never available due to range heterogeneities. The different range cells used for estimating the covariance matrix are not iid due to range attenuation effects and the simple fact that some areas will not have the same statistical properties over several km. Additionally for Reed's Rule to hold, twice the number of DOF iid sample support must be used further complicating the sample support and computational complexity problems.

2.5 PAMF

The PAMF uses a multichannel AR model and achieves the clutter and interference suppression desired by traditional STAP algorithms without the massive secondary support requirements. AR models are a subclass of parametric model based estimation that assume information about the random process. These inherent assumptions reduce the amount of required estimation data [11].

The primary advantage is the ability to provide $N(M - Z)$ DOF, close to *full adaptivity* or NM DOF, with small sample support requirements. The variable Z is the AR estimating filter order [18], where typically $Z \ll M$. Other reduced sample support methods provide far fewer DOF because of the sample requirements associated with the full rank covariance matrix estimate.

The covariance matrix $\mathbf{R}$ can be represented using a block matrix Lower Diagonal Lower (LDL) decomposition, where $\mathbf{R} = \mathbf{A}\mathbf{D}\mathbf{A}^H$ [14]. The matrix $\mathbf{A}$ has dimensions $MN \times MN$ with an inverse given by

$$\begin{bmatrix} \mathbf{I}_N & \mathbf{0} & \dots & \mathbf{0} \\ \mathbf{A}_1^H(1) & \mathbf{I}_N & \dots & \mathbf{0} \\ \mathbf{A}_2^H(2) & \mathbf{A}_2^H(1) & \dots & \mathbf{0} \\ \vdots & \vdots & \ddots & \vdots \\ \mathbf{A}_{M-1}^H(M-1) & \mathbf{A}_{M-2}^H(M-2) & \dots & \mathbf{I}_N \end{bmatrix}, \tag{2.29}$$

where $\mathbf{I}_N$ is a $N \times N$ identity matrix, $\mathbf{0}$ is a matrix of zeros of size $N \times N$, and $\mathbf{A}_i^H(i)$ represents the i^{th} order AR filter coefficients used in linear prediction under known covariance.

Under *known* interference statistics, an LDL decomposition of the covariance matrix $\mathbf{R}$ provides the AR filter coefficients. As a result the parametric filter coefficients $\mathbf{A}_i^H$ are known and the resultant PAMF output SINR is mathematically equivalent to the MF originally developed in [12].

This block decomposition provides the underlying PAMF justification. This interpretation allows another method for whitening the interference returns: estimate reduced order parametric filter coefficients instead of the covariance matrix. This simple fact means the PAMF does not follow Reed's Rule [15] and required sample support is *not* twice the DOF.

There are several different parameter estimation algorithms available in the literature. This thesis uses the Levinson-Wiggins-Robinson Recursion estimation algorithm in Appendix A [19]. Additional multichannel parameter estimation theory and algorithms can be found in [20].

After the prediction error filter coefficients have been estimated for each sample support range cell, the PAMF whitens the data using the filter coefficients averaged across the sample support range cells. For analytical convenience, a block matrix $\mathbf{B}_{np}$ with dimensions $N(M-Z) \times NM$ is defined as [14]

$$\begin{bmatrix} \mathbf{A}_2^H(2) & \mathbf{A}_2^H(1) & \mathbf{I}_N & \mathbf{0} & \dots & \mathbf{0} \\ \mathbf{0} & \mathbf{A}_2^H(2) & \mathbf{A}_2^H(1) & \mathbf{I}_N & \dots & \mathbf{0} \\ \mathbf{0} & \mathbf{0} & \mathbf{A}_2^H(2) & \mathbf{A}_2^H(1) & \dots & \mathbf{0} \\ \vdots & \ddots & \vdots & \vdots & \ddots & \vdots \\ \mathbf{0} & \dots & \mathbf{0} & \mathbf{A}_2^H(2) & \mathbf{A}_2^H(1) & \mathbf{I}_N \end{bmatrix}. \tag{2.30}$$

The block vector residual $\boldsymbol{\epsilon}$ can be viewed as the output of a Moving Average (MA) filter using the estimated prediction error coefficients,

$$\boldsymbol{\epsilon} = \mathbf{B}_{np}\boldsymbol{\chi}, \tag{2.31}$$

where $\boldsymbol{\chi}$ is again the received radar space-time snapshot. Define the residual covariance matrix as

$$\mathbf{R}_\epsilon = \varepsilon[\boldsymbol{\epsilon}\boldsymbol{\epsilon}^H]. \tag{2.32}$$

Following the development in [18], define a Hermitian matrix $\mathbf{C}$ as

$$\mathbf{C} = \mathbf{B}_{np}^H[\mathbf{I}_{N-Z} \otimes \mathbf{R}_\epsilon^{-1}]\mathbf{B}_{np}, \tag{2.33}$$

where $\otimes$ is the Kronecker product defined in [9]. Finally, the PAMF weight vector is

$$\mathbf{w}_{\text{PAMF}} = \frac{\mathbf{C}\mathbf{v}}{\sqrt{\mathbf{v}^H\mathbf{C}\mathbf{v}}}, \tag{2.34}$$

where $\mathbf{v}$ is the space-time steering vector of [2]. The true strength of the PAMF shows itself in Chapter V in Monte Carlo analysis under unknown interference statistics.

2.6 Summary

Chapter II presents the current state of the art for sidelooking STAP techniques. The literature review allows a comparison between published sidelooking array work and forward looking array work in the following chapters. This chapter first provides a generic airborne radar problem overview. After the problem overview, Section 2.2 reviews the published sidelooking array data model with added clutter decorrelation effects. Then, Section 2.3 goes over the basic background on STAP and Sections 2.4 and 2.5 show some of the implementation issues for STAP. After understanding the sidelooking data model, the more difficult forward looking problem is ready to be discussed.

III. Forward Looking Radar Modelling

The forward looking radar data model builds upon the sidelooking array data model introduced in Chapter II. This area represents a void in the available literature and is ripe for potential applications because most aircraft have forward looking arrays [1].

Once this forward looking radar data model is established, a comparison to the sidelooking configuration is offered in Chapter IV. This comparison addresses the different clutter spectral shapes and the associated loss of homogeneity. Chapter V examines radar performance when limited to a linear array allowing only azimuth and Doppler adaptivity, i.e., two-dimensional (2D) target localization. This chapter illustrates the limited capability to counter the increased interference environment associated with the forward looking system. Chapter VI evaluates an extension to include three-dimensional (3D) adaptivity and illustrates a significant performance improvement.

The current chapter builds a forward looking radar model from fundamental principles. The radar waveform is examined within the context of transmission and reflection from a single point scatterer. From this basic single point scatterer return, an entire interference environment is formed within a statistical context based on physical constraints.

Section 3.2 addresses this identical problem within the context of a well known sidelooking radar data model but using a 90° crab angle to simulate the forward looking case. As Section 3.3 shows, this second approach is mathematically equivalent to the first.

The final section introduces decorrelation effects, making the model more reflective of real world radar and antenna conditions. As shown in subsequent chapters and real world data, decorrelation effects significantly degrade nominal radar detection performance.

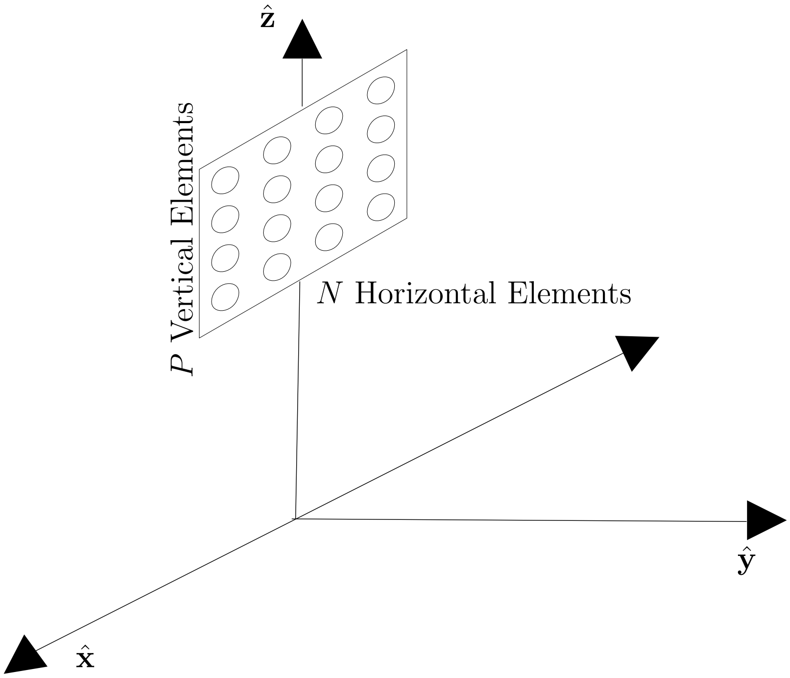

Figure 3.1: Planar array model with P vertical elements spaced d_z apart and N horizontal elements spaced d_x apart. The velocity vector is now oriented along the y-axis.

3.1 Forward Looking Model

The airborne radar considered in this section is pulsed as described in [6]. The velocity vector in the forward looking array case lies along the positive y-axis. The radar antenna array consists of P stacked linear arrays with N elements. The linear arrays extend along the x-axis and P of them are placed along the z-axis. These elements are equidistantly separated along the x and z axes with distances d_x and d_z, respectively. Figure 3.1 illustrates this array configuration.

The following mathematical development parallels that of [2] and [3]. The development deviates from these models in the velocity vector's orientation with respect to array boresight, i.e., from a side looking to a forward looking configuration. Since the velocity vector is the only factor to change from Chapter II, only model characteristics dependent on the velocity, i.e. the clutter, change.

3.1.1 Transmitted Waveform.

The transmitted radar waveform is described by

$$s(t) = a_t u(t) e^{j(\omega_o t + \psi)}, \tag{3.1}$$

where a_t is the transmitted pulse amplitude, $u(t)$ is the pulse train, ω_o is carrier frequency in radians, and ψ is a random starting phase. The pulse train is composed of M fundamental pulses $u_p(t)$ and is given by

$$u(t) = \sum_{m=0}^{M-1} u_p(t - mT_r), \tag{3.2}$$

where T_r is the Pulse Repetition Interval (PRI).

3.1.2 Received Waveform.

In the same way, the received waveform at element np has the same general form as Eqn. (2.8). The total delay time to element np equals the delay due to the round trip time, τ_t, plus the delay from element np to the first element to receive the signal return, τ'_{np}. This total delay is represented as

$$\tau_{np} = \tau_t + \tau'_{np}, \tag{3.3}$$

where the round trip delay time is simply $\tau_t = \frac{2R_t}{c}$ [8]. R_t is the range to the target and c is the propagation speed of the radar waveform, the speed of light. The delay to element np is

$$\tau'_{np} = \frac{-\hat{\mathbf{k}}(\theta, \phi) \bullet \mathbf{d}_{np}}{c}, \tag{3.4}$$

where $\mathbf{d}_{np}$ is described in Eqn. (2.3). Simplifying Eqn. (3.4) results in

$$\tau'_{np} = \frac{-nd_x \cos(\theta_t)\sin(\phi_t) - pd_z \sin(\theta_t)}{c}. \tag{3.5}$$

The actual phase delay from the first element to receive the radar signal to the np^{th} element is equal to

$$-w_o\tau'_{np} = \frac{2\pi f_o[nd_x\cos(\theta_t)\sin(\phi_t) + pd_z\sin(\theta_t)]}{c}. \tag{3.6}$$

The target spatial frequency is defined to simplify the phase delay as

$$\vartheta_t = \frac{\hat{\mathbf{k}}(\phi_t, \theta_t) \bullet \mathbf{d}_{np}}{\lambda_o}. \tag{3.7}$$

After carrying out the dot product, the target spatial frequency can be represented as

$$\vartheta_t = \frac{nd_x\cos(\theta_t)\sin(\phi_t) + pd_z\sin(\theta_t)}{\lambda_o}. \tag{3.8}$$

The target spatial frequency is then divided into the x-axis and z-axis components for analytical simplification,

$$\vartheta_x = \frac{d_x\cos(\theta_t)\sin(\phi_t)}{\lambda_o} \tag{3.9}$$

$$\vartheta_z = \frac{d_z\sin(\theta_t)}{\lambda_o}. \tag{3.10}$$

The phase delay can now be expressed using the target spatial frequencies as

$$-w_o\tau'_{np} = 2\pi(n\vartheta_x + p\vartheta_z). \tag{3.11}$$

Now, the received signal can be written as

$$s_{np}(t) = a_r u(t - \tau'_{np} - \tau_t)e^{j2\pi f_o(t-\tau'_{np}-\tau_t)}e^{j2\pi f_t(t-\tau'_{np}-\tau_t)}e^{j\psi}, \tag{3.12}$$

but τ'_{np} is significantly less than the envelope pulse width so τ'_{np} can be reasonably ignored in $u(t)$. Also, using the target spatial frequencies, $e^{-j2\pi f_o\tau'_{np}} = e^{j2\pi(n\vartheta_x+p\vartheta_z)}$. Finally, the exponentials that are not functions of time or the parameters n and p

are incorporated into the random phase term with no loss of information. These three simplifications reduce the received signal to

$$s_{np}(t) \cong a_r u(t-\tau_t) e^{j2\pi f_o t} e^{j2\pi f_t t} e^{j\psi} e^{j2\pi(n\vartheta_x + p\vartheta_z)}. \tag{3.13}$$

3.1.3 Receiver Processing. To make the processing easier, the signal is down converted to baseband so the signal is now

$$s_{np}(t) \cong a_r u(t-\tau_t) e^{j2\pi f_t t} e^{j\psi} e^{j2\pi(n\vartheta_x + p\vartheta_z)}. \tag{3.14}$$

The down converter filter is assumed to not pass the carrier frequency image frequencies [21]. Matched filters, used in radar, convolve the received signal with the filter's impulse response. The matched filter output is

$$\chi_{np} = \int_{-\infty}^{\infty} s_{np}(\tau) h(t-\tau) d\tau, \tag{3.15}$$

with the impulse response, $h(t) = u_p^*(-t)$. The matched filter output can be expressed as

$$\begin{aligned}\chi_{np} &\cong \int_{-\infty}^{\infty} a_r u(\tau-\tau_t) e^{j2\pi f_t \tau} e^{j\psi} e^{j2\pi(n\vartheta_x + p\vartheta_z)} u_p^*(\tau - t) d\tau \\ &\cong a_r e^{j2\pi(n\vartheta_x + p\vartheta_z)} e^{j\psi} \int_{-\infty}^{\infty} \sum_{m=0}^{M-1} u_p(\tau - \tau_t - mT_r) u_p^*(\tau - t) e^{j2\pi f_t \tau} d\tau,\end{aligned} \tag{3.16}$$

where $u(t)$ from Eqn. (2.5) has been used. The next step is to define a change of variables, $z = \tau - mT_r$. Therefore, the substitution $\tau = z + mT_r$ is used in Eqn. (3.16) obtaining,

$$\chi_{np} \cong a_r e^{j2\pi(n\vartheta_x + p\vartheta_z)} e^{j\psi} \sum_{m=0}^{M-1} e^{j2\pi f_t m T_r} \int_{-\infty}^{\infty} u_p(z - \tau_t) u_p^*(-t + z + mT_r) e^{j2\pi f_t z} dz. \tag{3.17}$$

The integral term in the equation above is a form of the Time-Frequency Auto-Correlation Function (TFACF) [22]. As long as the radar waveforms remain Doppler tolerant, the integral term approximately equals one. Doppler tolerance means a small shift in time in the TFACF does not cause a large Doppler frequency shift [6]. Due to the Doppler effect, the received signal envelope is actually stretched or compressed causing a time mismatch in the matched filter [10]. According to Klemm [1], the mismatch effect is minimal as long as long as $2v_r f_o \leq cB$, where B is the bandwidth. This condition is a reasonable assumption for most realistic target velocities and bandwidths and therefore the radar waveform is considered Doppler tolerant. Thus, the received signal at element np is

$$\chi_{np} \cong a_r e^{j\psi} e^{j2\pi(n\vartheta_x + p\vartheta_z)} \sum_{m=0}^{M-1} e^{j2\pi\bar{\omega}_t m}, \tag{3.18}$$

where the substitution $\bar{\omega}_t = f_t T_r$ is used. The data received at each element represents a coherent integration of the M pulses in a Coherent Processing Interval (CPI). The return from pulse m at element np for a given range cell is

$$\chi_{mnp} \cong \alpha_t e^{j2\pi(n\vartheta_x + p\vartheta_z)} e^{j2\pi\bar{\omega}_t m}, \tag{3.19}$$

where $\alpha_t = a_r e^{j\psi}$.

3.1.4 Block Data Format.

After the radar signal has been received, down converted, and match filtered, the data needs to be put into some mathematical format suitable for customary linear algebra operations. This formatting is accomplished using the Kronecker product [9]. First, consider all the returns from the N azimuth antenna elements in a concatenated vector for a given range cell,

$$\boldsymbol{\chi}_{mp} = \alpha_t e^{j2\pi m\bar{\omega}_t} e^{j2\pi p\vartheta_z} \begin{bmatrix} 1 & e^{j2\pi\vartheta_x} & \dots & e^{j2\pi(N-1)\vartheta_x} \end{bmatrix}^T. \tag{3.20}$$

Noticing the column vector has a special format to it, define the azimuth steering vector $\mathbf{a}$ as

$$\mathbf{a}(\vartheta_x) = \begin{bmatrix} 1 & e^{j2\pi\vartheta_x} & \dots & e^{j2\pi(N-1)\vartheta_x} \end{bmatrix}^T. \tag{3.21}$$

Following the development in [3] used for sidelooking arrays, the temporal steering vector $\mathbf{b}$ and the elevation steering vector $\mathbf{e}$ are defined as

$$\mathbf{b}(\bar{\omega}_t) = \begin{bmatrix} 1 & e^{j2\pi\bar{\omega}_t} & \dots & e^{j2\pi(M-1)\bar{\omega}_t} \end{bmatrix}^T \tag{3.22}$$

$$\mathbf{e}(\vartheta_z) = \begin{bmatrix} 1 & e^{j2\pi\vartheta_z} & \dots & e^{j2\pi(P-1)\vartheta_z} \end{bmatrix}^T. \tag{3.23}$$

Using these steering vectors, the data is formatted as follows below,

$$\boldsymbol{\chi}_{mp} = \alpha_t e^{j2\pi m\bar{\omega}_t} e^{j2\pi p\vartheta_z} \mathbf{a}(\vartheta_x). \tag{3.24}$$

Also, NM returns from the p^{th} elevation bank are expressed as

$$\boldsymbol{\chi}_p = \alpha_t e^{j2\pi p\vartheta_z} \mathbf{b}(\bar{\omega}_t) \otimes \mathbf{a}(\vartheta_x), \tag{3.25}$$

where $\otimes$ represents the Kronecker product. Finally, the 3D space-time snapshot χ_t for a given range cell is

$$\boldsymbol{\chi}_t = \alpha_t \mathbf{e}(\vartheta_z) \otimes \mathbf{b}(\bar{\omega}_t) \otimes \mathbf{a}(\vartheta_x). \tag{3.26}$$

The 3D steering vector $\mathbf{v}_t$ has the same form as it did for the sidelooking array case,

$$\mathbf{v}_t = \mathbf{e}(\vartheta_z) \otimes \mathbf{b}(\bar{\omega}_t) \otimes \mathbf{a}(\vartheta_x). \tag{3.27}$$

The space-time steering vector physically represents the phase changes on every channel and pulse return for a single point scatterer at some location in elevation, azimuth, and normalized Doppler referenced to one of the elements and pulses within the CPI [10]. Using the steering vector, the space-time snapshot can be represented as

$$\boldsymbol{\chi}_t = \alpha_t \mathbf{v}_t. \tag{3.28}$$

The space-time snapshot physically represents the return from a single point scatterer.

In real radar systems, the return due to the target $\boldsymbol{\chi}_t$ has to compete with undesirable returns. Hence, the received data is represented as

$$\boldsymbol{\chi} = \boldsymbol{\chi}_t + \boldsymbol{\chi}_u, \tag{3.29}$$

where the undesirable returns $\boldsymbol{\chi}_u$ are composed of thermal noise, barrage noise jamming, and clutter. This model uses a single point scatterer for the target return and therefore needs to add in thermal noise, jamming, and clutter to the data.

3.1.5 Thermal Noise Model. Only white Gaussian thermal noise is assumed present in the data. This noise is internally generated by the receivers, and given every element has its own receiver, the noise is mutually independent for every element. The correlation matrix for the noise component is defined as

$$\mathbf{R}_n = \varepsilon[\boldsymbol{\chi}_n \boldsymbol{\chi}_n^H]. \tag{3.30}$$

The correlation matrix for independent random processes is the identity matrix [11]. The thermal noise is assumed to be zero mean, since there is no direct current component within the return. For zero mean random processes, the covariance matrix is equal to the correlation matrix. Therefore, the noise covariance matrix is equal to

$$\mathbf{R}_n = \sigma^2 \mathbf{I}_{MNP}, \tag{3.31}$$

where σ^2 is the noise power and $\mathbf{I}_{MNP}$ is an identity matrix with dimensions $MNP \times MNP$. It is important to note the thermal noise guarantees the covariance matrix is non-singular.

3.1.6 Jammer Model. This thesis only takes into account noise jamming. Noise jammer signals are uncorrelated temporally but correlated spatially. The spatial correlation property means that returns are correlated across the array. Similarly, the temporal uncorrelated property means that the returns are uncorrelated from pulse to pulse. The jamming signals are also assumed to be zero mean so that the covariance matrix is equivalent to the correlation matrix. Using the properties of the Kronecker product and following the process as done by [3], the jammer covariance matrix is

$$\mathbf{R}_j = \sigma^2 \xi_j \mathbf{e}(\vartheta_z)\mathbf{e}^H(\vartheta_z) \otimes \mathbf{I}_M \otimes \mathbf{a}(\vartheta_x)\mathbf{a}^H(\vartheta_x), \tag{3.32}$$

where ξ_j is the Jammer to Noise Ratio (JNR). The JNR equals $\frac{J_o}{N_o}$, where J_o is the two-sided jammer Power Spectral Density (PSD) that is received and N_o is the two-sided noise PSD. The jammer PSD is

$$J_o = \frac{S_j g(\phi, \theta) \lambda_o^2}{(4\pi R_j)^2 L_r}, \tag{3.33}$$

where S_j is the effective jammer radiated PSD that is transmitted, $g(\phi, \theta)$ is the element gain, R_j is the range to the jammer, and L_r is the receiver loss.

3.1.7 Clutter Model. The airborne clutter model established by [3] takes into account ambiguous clutter returns and planar arrays. This model is an extension to the physical model developed by [2] with added decorrelation effects by [1] and [4].

Since ground returns are typically much larger than sky clutter, any sky clutter returns have been ignored. A 4/3 effective radius is used to model the earth as a sphere.

Due to range ambiguities associated with pulsed radar signals, the radar receives clutter returns for the same range cell at multiples of the unambiguous range up to the horizon range. Each range ring consists of clutter patches with a certain RCS and grazing angle as discussed in [6].

The clutter Doppler frequency at any patch is

$$f_c(\theta_i, \phi_k) = \frac{2\hat{\mathbf{k}}(\theta_i, \phi_k) \bullet \mathbf{v}_a}{\lambda_o}. \tag{3.34}$$

Remembering that the velocity vector is totally along the y-axis (assuming no crab angle) means the clutter Doppler frequency becomes

$$f_c^{FL}(\theta_i, \phi_k) = \frac{2v_a \cos(\theta_i) \cos(\phi_k)}{\lambda_o}. \tag{3.35}$$

Notice the clutter in the forward looking array case is range dependent, because the clutter null is at different frequencies for different ranges. The clutter returns are assumed to be zero mean so that the covariance matrix is equal to the correlation matrix. The clutter covariance matrix can be written as

$$\mathbf{R}_c = \sigma^2 \sum_{i=1}^{N_c} \sum_{k=1}^{N_r} \xi_{ik} \mathbf{e}(\vartheta_z) \mathbf{e}^H(\vartheta_z) \otimes \mathbf{b}(\bar{\omega}_{ik}) \mathbf{b}^H(\bar{\omega}_{ik}) \otimes \mathbf{a}(\vartheta_x) \mathbf{a}^H(\vartheta_x), \tag{3.36}$$

where ξ_{ik} is the Clutter to Noise Ratio (CNR), N_c is the number of clutter patches, and N_r is the number of ambiguous range rings. The number of ambiguous range rings is

$$N_r = \left\lfloor \frac{R_h}{R_u} \right\rfloor, \tag{3.37}$$

where R_h is the range to the horizon, R_u is the unambiguous range, and $\lfloor \ \rfloor$ is the floor function that rounds down to the next integer. From [6], the unambiguous range is

$$R_u = \frac{cT_r}{2}. \tag{3.38}$$

Following the development in [3], the range to the horizon is

$$R_h = \sqrt{h_a^2 + 2h_a a_e}, \tag{3.39}$$

where h_a is the height of the aircraft and a_e is the effective radius of the earth. The CNR for each patch is

$$\xi_{ik} = \frac{P_t G(\theta_i, \phi_k) g(\theta_i, \phi_k) \lambda_o^2 \sigma_{ik}}{(4\pi)^3 N_o B L_s R_i^4}, \tag{3.40}$$

where P_t is the transmit power, $G(\theta_i, \phi_k)$ is the array gain, $g(\theta_i, \phi_k)$ is the element gain, σ_{ik} is the clutter patch effective radar cross section, L_s is the system loss, and R_i is the range to the clutter patch. The clutter patch effective radar cross section is defined by the constant gamma model [6],

$$\sigma_{ik} = \gamma \sin(\psi_i) R_i \Delta\phi \Delta R \sec(\psi_i), \tag{3.41}$$

where γ is the value that defines the constant gamma model, ψ_i is the grazing angle from Fig. 2.5, R_i is the range to the clutter patch, $\Delta\phi$ equals $2\pi/N_c$ and ΔR equals the range resolution $c/2B$.

> $\boxed{!}$ An important point to make is that for ranges less than the altitude, only ambiguous clutter returns are present.

3.1.8 Total Interference plus Noise Covariance Matrix. The next step consolidates the different components into the total covariance matrix. Typically, radar returns are assumed to be one of two hypotheses. The H_1 hypothesis is

$$\boldsymbol{\chi} = \boldsymbol{\chi}_t + \boldsymbol{\chi}_c + \boldsymbol{\chi}_n + \boldsymbol{\chi}_j, \tag{3.42}$$

which means that the target is present. The H_0 hypothesis occurs when no target is present, that is

$$\boldsymbol{\chi} = \boldsymbol{\chi}_c + \boldsymbol{\chi}_n + \boldsymbol{\chi}_j. \tag{3.43}$$

The total covariance matrix is computed under the H_0 hypothesis

$$\mathbf{R} = \varepsilon[\boldsymbol{\chi}\boldsymbol{\chi}^H] = \mathbf{R}_c + \mathbf{R}_j + \mathbf{R}_n, \tag{3.44}$$

where $\mathbf{R}$ is the interference plus noise covariance matrix and assuming that the noise, jammer, and clutter returns are all mutually uncorrelated. The covariance matrix has dimensions $MNP \times MNP$ and is full rank due to the white noise component.

> ! The ambiguous clutter returns that this model incorporate are very important for forward looking radar because the ambiguous returns cause multiple clutter nulls and increase the rank of the clutter covariance matrix.

3.2 Sidelooking Data Model with 90° Crab Angle

The data model reviewed in Chapter II for sidelooking arrays is now modified to have a 90° crab angle. The crab angle directs the aircraft velocity vector towards the positive y-axis along the array boresight angle. Therefore, the velocity vector is expressed as

$$\mathbf{v}_a = v_a \hat{\mathbf{y}}, \tag{3.45}$$

where v_a is the aircraft's speed directed in the positive y-axis. The clutter Doppler spectrum as already given in Eqn. (2.17) is

$$f_c(\theta_i, \phi_k) = \frac{2\hat{\mathbf{k}}(\theta_i, \phi_k) \bullet \mathbf{v}_a}{\lambda_o}, \tag{3.46}$$

where λ_o is the wavelength, and $\hat{\mathbf{k}}(\theta_i, \phi_k)$ is the unit vector in angular radar coordinates. The unit vector from Eqn. (2.2) is equal to

$$\hat{\mathbf{k}}(\phi, \theta) = \cos(\theta)\sin(\phi)\hat{\mathbf{x}} + \cos(\theta)\cos(\phi)\hat{\mathbf{y}} + \sin(\theta)\hat{\mathbf{z}}. \tag{3.47}$$

Using the unit vector and aircraft velocity, the clutter Doppler reduces to

$$f_c^{FL}(\theta_i, \phi_k) = \frac{2v_a\cos(\theta_i)\cos(\phi_k)}{\lambda_o}. \tag{3.48}$$

Therefore, the clutter ridge for forward looking arrays implemented using a 90° crab angle is not linear with $\sin(\phi)$. In fact, it is nonlinear because two different azimuth angles produce the same Doppler frequency.

3.3 Equivalence

This section shows the equivalence of the two methods used to generate the forward looking array data model. The first technique is the velocity vector pointing out along the planar array boresight and the second technique is the 90° crab angle on the sidelooking array data model. The equivalence is shown by pointing out the two techniques result in identical total interference plus noise covariance matrices.

First, the portion of the total covariance matrix due to receiver thermal noise, $\mathbf{R}_n$, is equal to $\sigma^2\mathbf{I}_{MNP}$ in both the sidelooking and forward looking cases as shown in Eqns. 2.15 and 3.31. Second, the jammer covariance matrix, $\mathbf{R}_j$ is also equivalent in both cases as shown in Eqns. 2.16 and 3.32. Third, the two different methods both give the same clutter-Doppler relationship as shown in Eqns. 3.48 and 3.35. Since the same azimuth, temporal, and elevation steering vectors are used to create the clutter covariance matrix, $\mathbf{R}_c$, the sidelooking with a 90° crab angle and forward looking array cases produce the same matrices. Therefore, the two different techniques give the same total interference plus noise covariance matrix, because the three undesirable covariance components are identical for both cases.

3.4 Decorrelation Effects

Decorrelation parameters take into account real world effects degrading radar performance. Clutter fluctuations are accounted for with Internal Clutter Motion (ICM). ICM accounts for foliage movement due to the wind within a clutter patch on a pulse-by-pulse basis. System Bandwidth accounts for spatial decorrelation across the array resulting from different propagation times on an element-by-element basis, when the clutter receive signal arrives at angles other than boresight. Standard array theory aligns receive signals on an element-by-element basis using phase delays. Therefore, the actual pulse envelope does not completely align at every element and a loss is incurred. Both decorrelation effects result in increased clutter covariance matrix rank. Figure 3.2 shows the increased clutter rank using eigenvalue analysis when both ICM and System Bandwidth are taken into account.

ICM fluctuations are assigned a Gaussian Doppler frequency spectrum. Hence, the temporal autocorrelation function is Gaussian as well [4]. The response from the i^{th} clutter patch at the k^{th} range ring can be expressed as

$$\boldsymbol{\chi}_c = \alpha_{ik}\mathbf{v}_{ik}, \tag{3.49}$$

where each patch is treated as a single point scatterer. The temporal autocorrelation can then be expressed as

$$\gamma(m) = \sigma^2 \xi_{ik} \exp\left(\frac{-B_c^2 m^2}{8}\right), \tag{3.50}$$

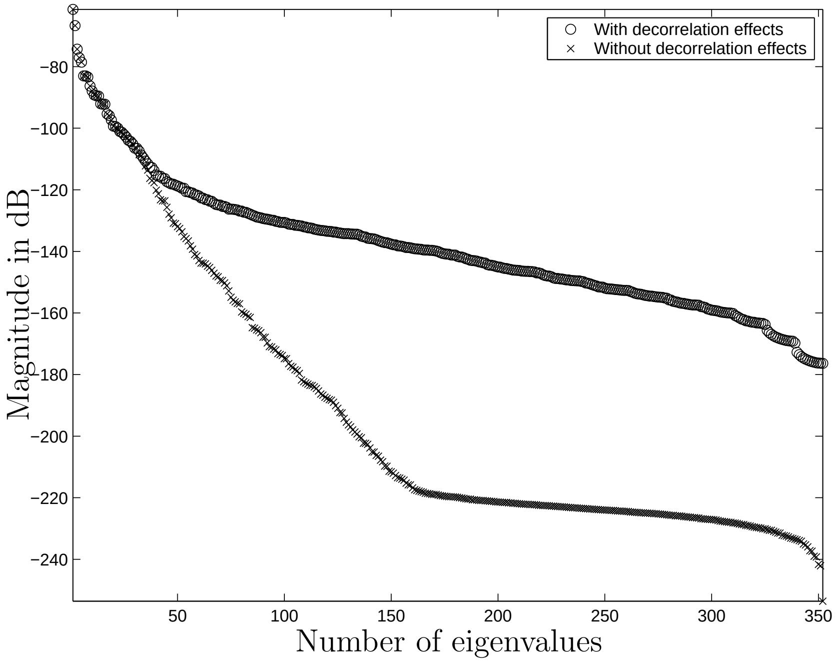

Figure 3.2: Increased clutter rank when decorrelation parameters are taken into account.

where B_c is the Gaussian spectral clutter bandwidth normalized by the PRF [1]. The clutter covariance matrix with ICM added can then be expressed as

$$\mathbf{R}_c = \sigma^2 \sum_{i=1}^{N_c} \sum_{k=1}^{N_r} \xi_{ik} \mathbf{e}(\vartheta_z)\mathbf{e}^H(\vartheta_z) \otimes [\mathbf{\Gamma}_{ICM} \odot \mathbf{b}(\bar{\omega}_{ik})\mathbf{b}^H(\bar{\omega}_{ik})] \otimes \mathbf{a}(\vartheta_x)\mathbf{a}^H(\vartheta_x), \quad (3.51)$$

where $\mathbf{\Gamma}_{ICM}$ is equal to the Toeplitz matrix of the vector $\begin{bmatrix}\gamma(0) & \dots & \gamma(M-1)\end{bmatrix}$ and $\odot$ is the Hadamard product. The Hadamard product is element-by-element multiplication. The Toeplitz function creates a Hermitian matrix from a vector where the first row and first column of the matrix are the vector elements. Figure 3.3 illustrates the correlation function for ICM. Notice the correlation function reverts back to 1 as B_c goes to 0. Therefore, setting B_c to 0 results in no ICM decorrelation effect. As B_c gets higher, the clutter returns are more uncorrelated and the clutter rank significantly increases.

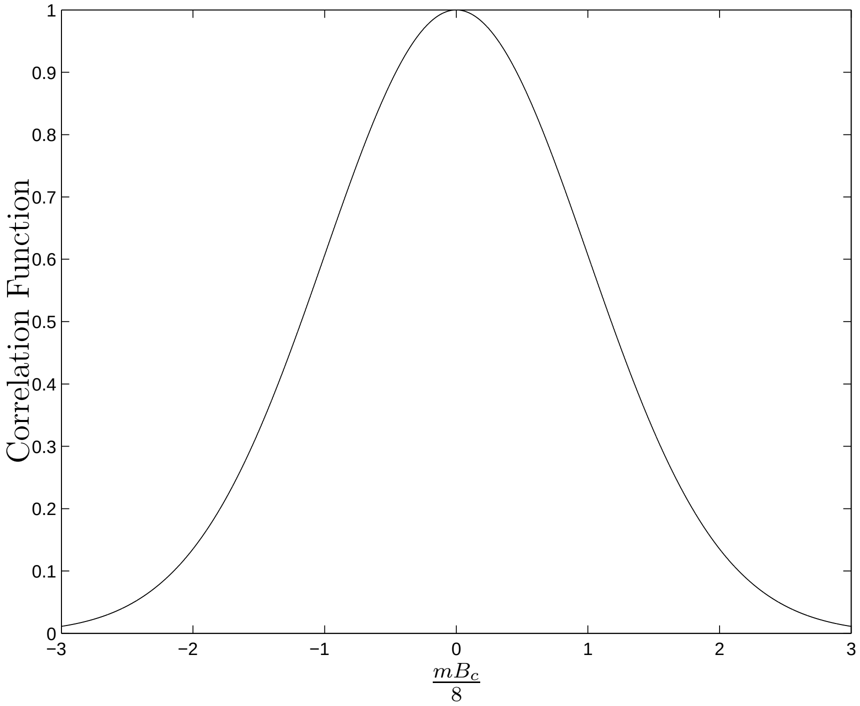

Figure 3.3: Correlation function for ICM decorrelation effects. Notice the correlation function equals 1 as B_c equals 0 representing no ICM decorrelation effect.

The System Bandwidth effect is a spatial decorrelation unlike ICM, a temporal decorrelation. This effect accounts for the difference in the expected time delay to element np because phase delays are used in the array processing. The carrier is modulated by a rectangular function so the spatial decorrelation autocorrelation function can be expressed as a triangle function or

$$\rho_{np} = 1 - \frac{\mid \tau'_{np} \mid}{T_p}, \tag{3.52}$$

where τ'_{np} is the travel time from the reference element to element np and $\mid \tau'_{np} \mid$ is always less than or equal to the pulse width, T_p [1]. Figure 3.4 shows the correlation function for System Bandwidth. Notice the correlation function approaches 1 as the pulse width gets larger and the correlation function gets smaller as the pulse width decreases, representing an increase in clutter rank as decorrelation increases.

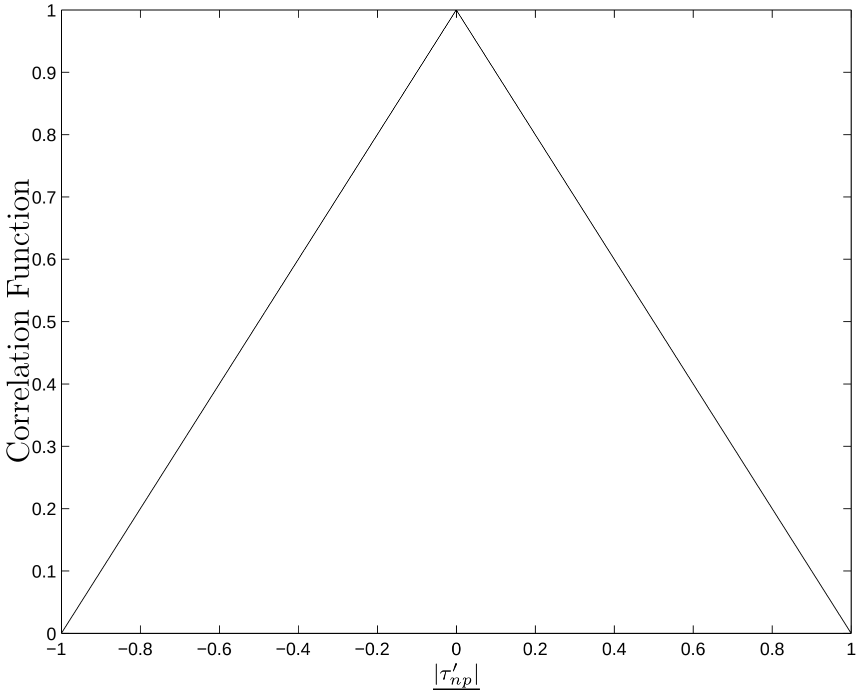

Figure 3.4: Correlation function for System Bandwidth decorrelation effects. Notice the correlation function gets larger as the pulse width increases representing a smaller System Bandwidth decorrelation effect.

The travel time due to the phase delay is described in Section 3.1.2, but is expressed here as

$$-\tau'_{np} = \frac{n\vartheta_x}{f_o} + \frac{p\vartheta_z}{f_o}, \tag{3.53}$$

where f_o is the radar transmit frequency. For analytical convenience, τ'_{np} is divided into two components below:

$$-\tau_x = \frac{n\vartheta_x}{f_o} \tag{3.54}$$

$$-\tau_z = \frac{p\vartheta_z}{f_o}. \tag{3.55}$$

They represent the x-axis and the z-axis time differences in the same manner that the spatial frequencies, ϑ_x and ϑ_z helped to ease the formatting of the data. Therefore, the clutter covariance matrix can be written as

$$\mathbf{R}_c = \sigma^2 \sum_{i=1}^{N_c} \sum_{k=1}^{N_r} \xi_{ik} [\mathbf{\Gamma}_{\mathrm{BW}z} \odot \mathbf{e}(\vartheta_z)\mathbf{e}^H(\vartheta_z)] \otimes [\mathbf{\Gamma}_{\mathrm{ICM}} \odot \mathbf{b}(\bar{\omega}_{ik})\mathbf{b}^H(\bar{\omega}_{ik})] \\ \otimes [\mathbf{\Gamma}_{\mathrm{BW}x} \odot \mathbf{a}(\vartheta_x)\mathbf{a}^H(\vartheta_x)], \quad (3.56)$$

where $\mathbf{\Gamma}_{\mathrm{BW}x}$ is the x-axis system bandwidth decorrelation matrix and $\mathbf{\Gamma}_{\mathrm{BW}z}$ is the z-axis system bandwidth decorrelation matrix. These two matrices are equal to

$$\mathbf{\Gamma}_{\mathrm{BW}x} = \mathrm{Toeplitz}\left[\rho_x(0) \quad \ldots \quad \rho_x(N-1)\right] \quad (3.57)$$

$$\mathbf{\Gamma}_{\mathrm{BW}z} = \mathrm{Toeplitz}\left[\rho_z(0) \quad \ldots \quad \rho_z(P-1)\right], \quad (3.58)$$

where $\rho_x(n) = 1 - \frac{n|\vartheta_x|}{T_p f_o}$ and $\rho_z(p) = 1 - \frac{p|\vartheta_z|}{T_p f_o}$. Note decorrelation effects are only applied to the clutter not to the noise and jammer.

3.5 Summary

Chapter III provides the forward looking radar data model used in the rest of this thesis. The forward looking radar model is developed from fundamental principles starting with the transmission and reflection from a single point scatterer. Using the well known sidelooking model from Chapter II with a 90° crab angle provides the same forward looking radar data model. Section 3.3 shows the different approaches are equivalent mathematically. The addition of decorrelation effects makes the model more indicative of real world radar performance. Decorrelation effects significantly degrade radar performance as shown in subsequent chapters.

Since this forward looking radar data model is established, a comparison to the sidelooking configuration is offered next in Chapter IV. This comparison addresses the different clutter spectral shapes and the associated loss of homogeneity in the forward looking case.

IV. Comparisons Between Forward and Sidelooking Arrays

This chapter compares and contrasts the sidelooking and forward looking array cases based on the data models introduced in Chapters II and III. These characteristics are compared using the Matched Filter (MF) and Noise limited cases.

After the comparisons are noted, Chapter V evaluates radar performance when limited to a linear array allowing only azimuth and Doppler adaptivity. This chapter illustrates the limited capability of linear arrays to mitigate the increased interference environment associated with the forward looking radar system. Chapter VI examines an extension to include three-dimensional adaptivity and illustrates a significant performance improvement in the forward looking case using planar arrays.

The current chapter discusses the general clutter-Doppler relationship and range cell homogeneity and notes the differences between the forward and sidelooking cases. The discussion on range cell homogeneity naturally leads into the difference in clutter ridge shape and clutter covariance matrix rank. Additionally, differences in clutter notches are noted between the two different array orientations.

Section 4.6 illustrates the degradation resulting from the addition of decorrelation parameters in the forward and sidelooking array cases.

The simulation parameters used in these comparisons are given in Table 4.1 unless otherwise noted.

4.1 Understanding the Clutter Environment

The generic clutter-Doppler relationship for any array orientation from Eqn. (2.17) equals

$$f_c(\theta_i, \phi_k) = \frac{2\hat{\mathbf{k}}(\theta_i, \phi_k) \bullet \mathbf{v}_a}{\lambda_o}. \tag{4.1}$$

Using this clutter-Doppler expression means the Doppler values can be evaluated as a function of every mainbeam direction, i.e., the sidelooking case corresponds to 0°

Table 4.1: Scenario parameters.

Variable	Value
M	32
N	11
P	1
f_o	1240 MHz
f_r	1984 Hz
T_p	0.8 μs
P_t	200 kW
B	800 kHz
F_n (Noise Figure)	3 dB
N_c	361
h_a (aircraft altitude)	3073 m
v_a (aircraft velocity)	$\frac{d_x f_r}{2}$
R	12 km
γ	-3 dB
Array Transmit Gain	22 dB
Element Pattern	Cosine
Element Gain	4 dB
Element Backlobe Level	-40 dB
d_x	0.10922 m
d_z	0.1407 m
Transmit Taper	Uniform (None)
System Losses L_s	3 dB
Target ϕ	0°
Target θ	0°
Target $\bar{\omega}$	0.25
B_c	$\frac{10}{f_r}$
ξ_t	1

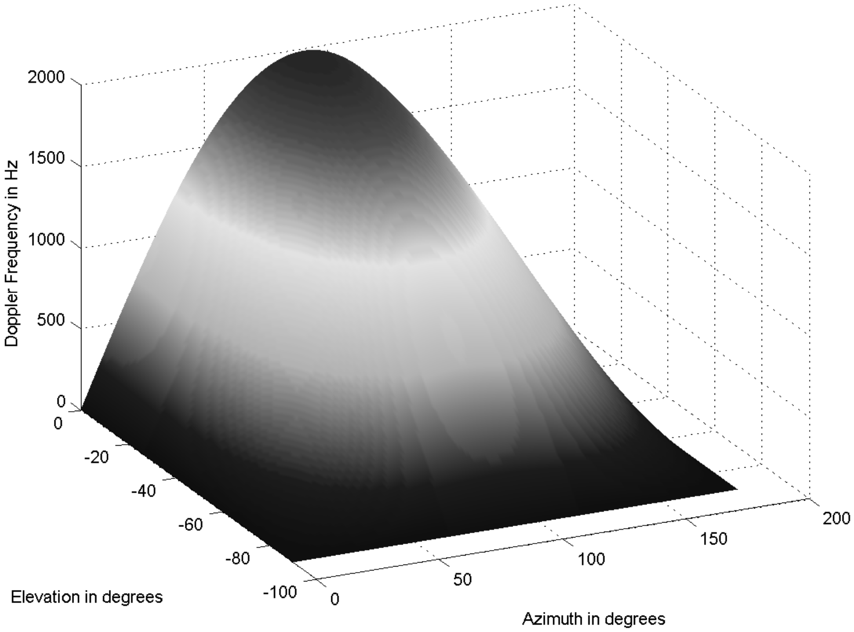

Figure 4.1: General clutter-Doppler values for any array orientation. Sidelooking arrays correspond to 0° azimuth and forward looking arrays correspond to 90° azimuth.

azimuth and the forward looking case corresponds to 90° azimuth. The 90° change between the two orientations in azimuth also explains why the $\sin(\phi)$ in Eqn. (4.4) changes into a $\cos(\phi)$ in Eqn. (4.2). Figure 4.1 shows the Doppler values for various mainbeam locations in ϕ and θ. Notice the Doppler value is 0 for 0° azimuth and remains constant versus θ for the side looking case. This lack of elevation dependency shows the range independence for mainbeam clutter in sidelooking radars. The Doppler values for 90° azimuth vary versus elevation and illustrate the range dependence for forward looking radar returns.

The clutter-Doppler frequency values in Fig. 4.1 show a bowl shape as discussed in [23]. The differences in range dependency for the forward and sidelooking array cases lead into the differences in homogeneity between the two cases.

4.2 Homogeneity

Space-Time Adaptive Processing (STAP) requires statistical sample support in order to estimate the interference environment. This statistical approach assumes Independent Identically Distributed (iid) data across range cells. When the sample support data is approximately iid, homogeneity is assumed. The lack of homogeneity is called heterogeneous data.

Sidelooking array sample support remains more homogeneous than forward looking array data because of range dependency effects. For the reader's convenience, the clutter-Doppler relationship for the forward looking case is given again from Eqn. (3.35) as

$$f_c^{FL}(\theta_i, \phi_k) = \frac{2v_a \cos(\theta_i)\cos(\phi_k)}{\lambda_o}. \tag{4.2}$$

By definition, every range cell occurs at different values of θ. This simple fact means every range cell has different Doppler characteristics and therefore the different range cells are *not* homogeneous in the forward looking case. Basically, forward looking clutter returns are range dependent and do not meet the iid criteria. Another viewpoint looks at the clutter-Doppler dependence on the x-axis and z-axis spatial frequencies from Eqn. (3.9) and Eqn. (3.10) as shown below

$$\begin{aligned} f_c^{FL}(\theta_i, \phi_k) &= \frac{2v_a \cos(\theta_i)\cos(\phi_k)}{\lambda_o} \\ &= \frac{2v_a \cos(\theta_i)\sqrt{1-\sin(\phi_k)^2}}{\lambda_o} \\ &= 2v_a\sqrt{\frac{\cos(\theta_i)^2\sin(\theta_i)^2 d_z^2}{\lambda_o^2 d_z^2 \sin(\theta_i)^2} - \frac{\cos(\theta_i)^2\sin(\phi_k)^2 d_x^2}{\lambda_o^2 d_x^2}} \\ &= 2v_a\sqrt{\frac{\cot(\theta_i)^2\vartheta_z^2}{d_z^2} - \frac{\vartheta_x^2}{d_x^2}}. \end{aligned} \tag{4.3}$$

Richardson notes the clutter-Doppler spectrum follows the shape of an ellipsoid when viewed as a function of the spatial frequencies [23].

Next, the sidelooking clutter-Doppler relationship from Eqn. (2.18) is given again as

$$f_c^{SL}(\theta_i, \phi_k) = \frac{2v_a \cos(\theta_i)\sin(\phi_k)}{\lambda_o}. \tag{4.4}$$

Since the main lobe is formed at 0° azimuth (assuming no crab angle), the clutter ridge always passes through 0 Hz because sin(0) is always 0 regardless of the range cell θ value. Consequently, the mainbeam clutter returns for sidelooking arrays are range independent and more homogeneous than the forward looking case. The clutter-Doppler can also be represented as a simple linear function of the x-axis spatial frequency

$$\begin{aligned} f_c^{SL}(\theta_i, \phi_k) &= \frac{2v_a \cos(\theta_i)\sin(\phi_k)}{\lambda_o} \\ &= \frac{2v_a d_x \cos(\theta_i)\sin(\phi_k)}{\lambda_o d_x} \\ &= \frac{2v_a \vartheta_x}{d_x}. \end{aligned} \tag{4.5}$$

Figure 4.2 illustrates the linear dependence existing the sidelooking array case between the clutter-Doppler and x-axis spatial frequency.

Clearly, the ellipsoid in the clutter-Doppler versus spatial frequency space for the forward looking case is significantly more complicated than the linear dependence existing in the clutter-Doppler versus x-axis spatial frequency for the sidelooking array case. Because the forward looking clutter-Doppler depends on the z-axis spatial frequency, every range cell possesses different clutter-Doppler characteristics depending on θ. Therefore, the forward looking array case is more heterogeneous than the sidelooking array case and fewer sample support is available for STAP algorithms that need iid support data.

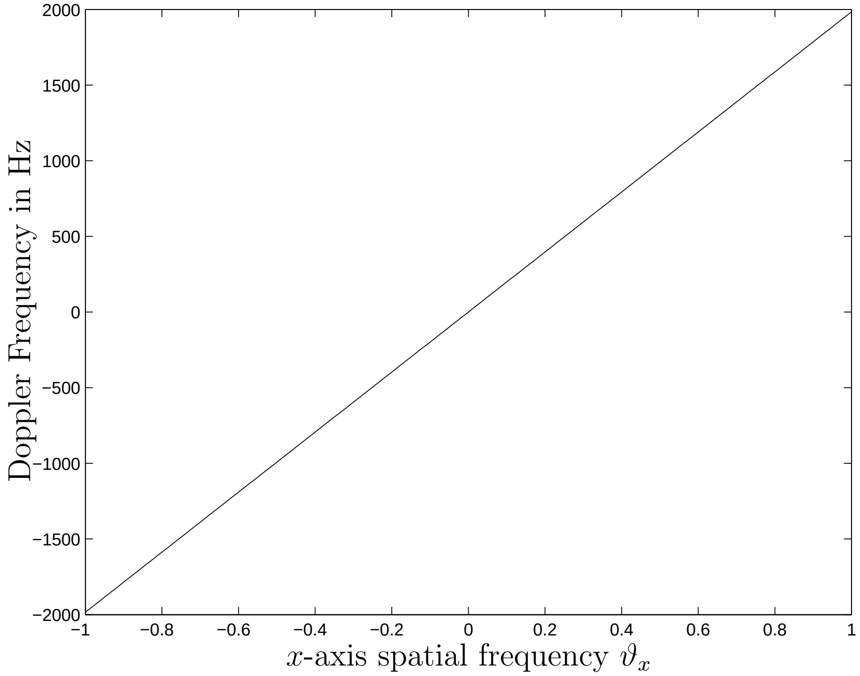

Figure 4.2: Linear dependence between clutter-Doppler and x-axis spatial frequency for a sidelooking array. The lack of dependence on the z-axis spatial frequency shows the main beam range independence for sidelooking arrays.

4.3 Clutter Ridges

The differences existing between the forward and sidelooking array cases with regards to homogeneity directly result in different clutter ridges. The sidelooking case clutter-Doppler relationship is linear with the sine of azimuth while the forward looking case clutter-Doppler relationship varies with the cosine of azimuth as shown in Eqn. (4.2) and Eqn. (4.4). The sidelooking array case clutter ridge is shown using the minimum variance representation of the Power Spectral Density (PSD) [1] for 12 km in Fig. 4.3. The sidelooking array case clutter properties remain more homogeneous across range cells as shown in Fig. 4.4 at 5 km. The clutter ridge for the sidelooking case always follows the same general shape regardless of the range in contrast with the range dependent forward looking case.

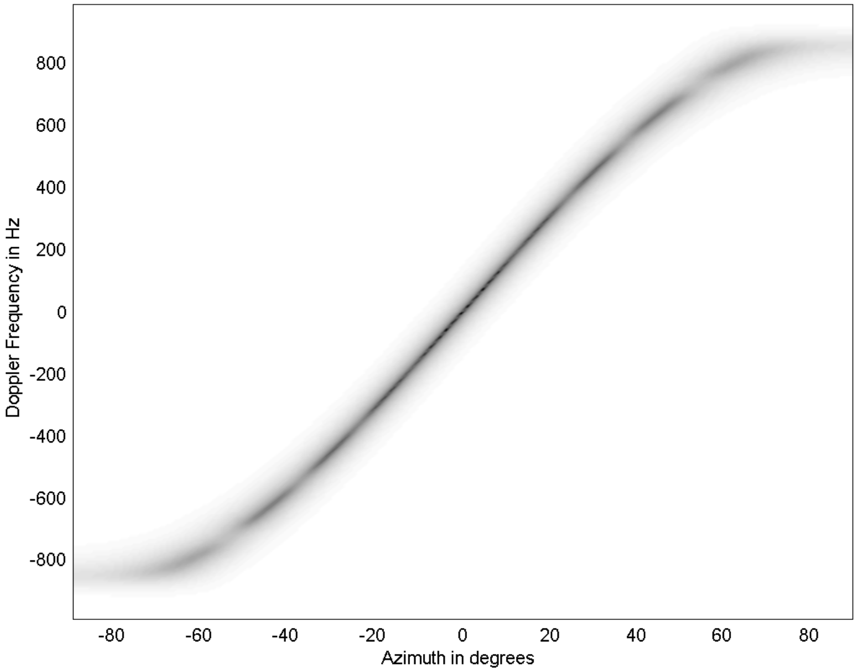

Figure 4.3: Clutter PSD for a sidelooking array at 12 km. Notice the variation versus $\sin(\phi)$ for sidelooking arrays.

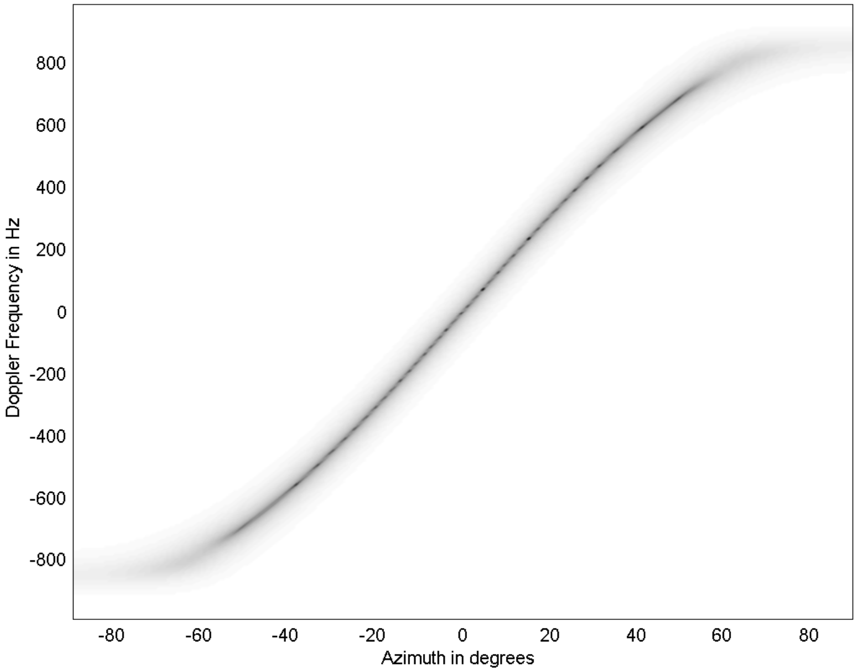

Figure 4.4: Clutter PSD for a sidelooking array at 5 km. Notice the clutter PSD is relatively unchanged from Fig. 4.3 at 12 km.

Figure 4.5 shows the forward looking array case clutter ridge using a PSD plot for 12 km. As noted in Section 4.2, the forward looking clutter properties change with range. Figure 4.6 illustrates the clutter spectral properties at 5 km for the forward looking case. STAP requires iid sample support to accurately estimate the interference environment, i.e. homogeneous data. As shown in Fig. 4.6, the interference environment significantly changes versus range in the forward looking radar case compared to Fig. 4.5 and performance will suffer from using the heterogeneous data as sample support. In fact, two noticeable clutter ridges exist at 5 km for the forward looking radar case but only one noticeable clutter ridge at 12 km.

This clutter-Doppler relationship for forward looking arrays results in several important ramifications. First, two azimuth angles produce the same Doppler frequency because cosine is an even function. Sidelooking arrays do not experience this phenomenon because for every azimuth angle there is one Doppler frequency and vice-versa. Second, multiple clutter ridges may appear due to range ambiguous clutter in the forward looking case but range ambiguous clutter does not cause additional clutter ridges in the sidelooking case.

4.4 Eigenvalue Analysis of Clutter Covariance Matrices

As a result of the differences between the forward looking and sidelooking array cases with regards to range dependency, clutter covariance matrices have different ranks for the forward and sidelooking array cases. Clutter covariance rank is an important concept because the higher the rank, the more difficult the interference suppression problem is [1]. As a result, interference suppression poses more difficulties in the forward looking case than it does for the sidelooking case. Eigenvalue analysis shows this difficulty because the number of eigenvalues is equal to the rank of the clutter covariance matrix. The increased rank for forward looking arrays arises from the ambiguous range clutter returns. The sidelooking case mainbeam

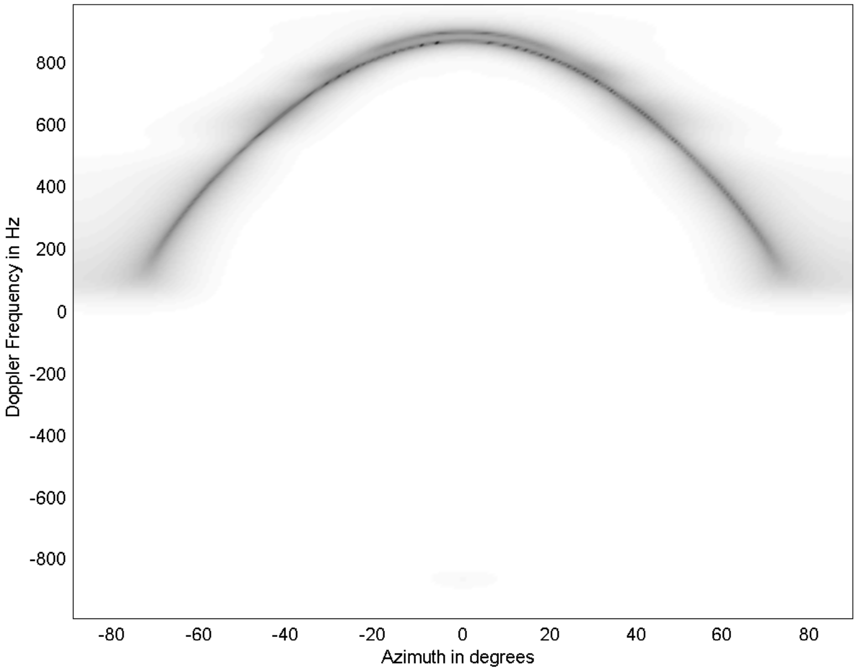

Figure 4.5: Clutter PSD for a forward looking array at 12 km. Notice the variation versus $\cos(\phi)$ for forward looking arrays.

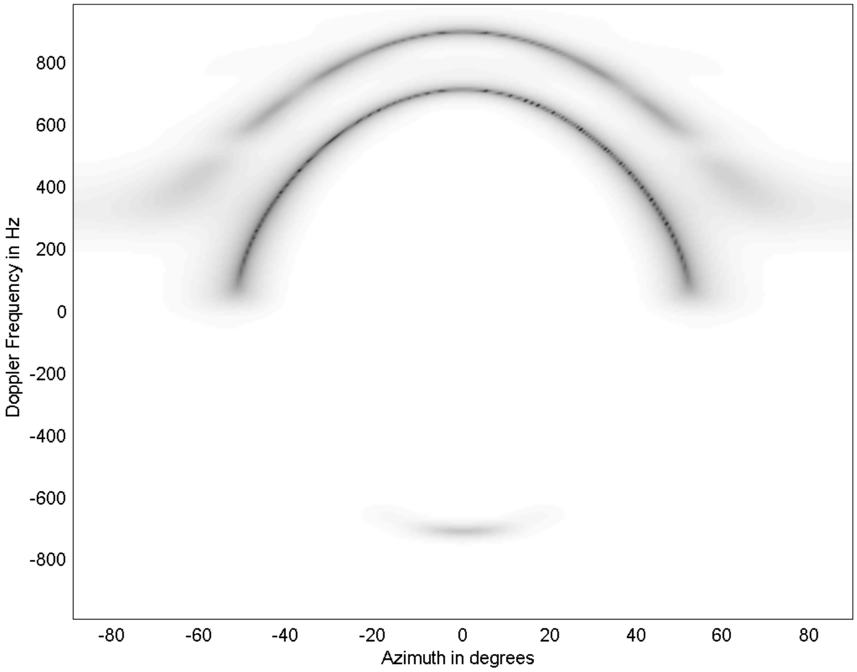

Figure 4.6: Clutter PSD for a forward looking array at 5 km. Notice the completely different clutter PSD for the forward looking case as compared to the clutter PSD in Fig. 4.5.

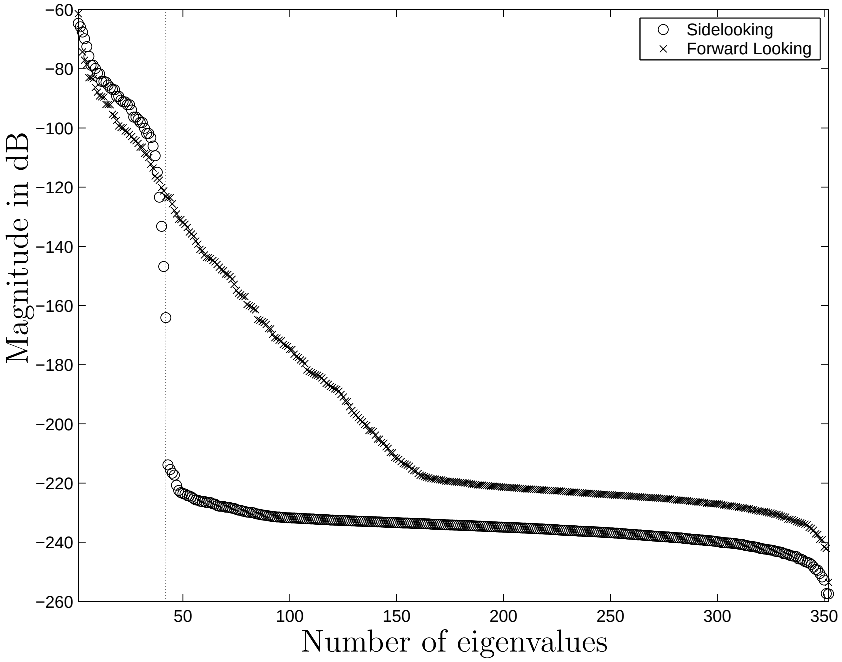

Figure 4.7: Eigenvalue Analysis for forward and sidelooking array cases. Notice the sidelooking array case clutter rank is significantly less than the forward looking array case because the range ambiguous clutter increases the clutter rank for the forward looking case.

clutter returns are range independent while the forward looking returns are range dependent.

Figure 4.7 shows a plot of the eigenvalues for the forward looking case and the sidelooking case. The rank of the clutter covariance matrix is 126 for the forward looking case. The difficulty in noticing the exact clutter rank occurs because the ambiguous clutter returns increase the rank of the clutter matrix but they have significantly less power than the unambiguous range ring. The clutter rank for linear sidelooking arrays is predicted by Brennan's Rule [24], which states the clutter rank is

$$r_c \approx \lfloor N + (M-1)\beta \rfloor. \tag{4.6}$$

In Eqn. (4.6), β is given as $\frac{2v_a T_r}{d_x}$. Brennan's rule has not been extended to planar arrays yet. For the values listed in Table 4.1, the clutter rank should be 42. Figure 4.7 shows Brennan's rule does indeed accurately predict the clutter rank for sidelooking linear arrays.

In this scenario, the reader should notice the forward looking array case clutter rank is three times the sidelooking array case clutter rank in this scenario. This fact can be explained because there are three total range rings (one unambiguous and two ambiguous). The ambiguous range rings increase the clutter rank for the range dependent forward looking case but not the sidelooking case. Next, the concept of clutter notches is discussed for forward and sidelooking array cases.

4.5 Clutter Notches

Sidelooking and forward looking arrays are very different with regards to clutter notches. Clutter notches are undesirable because they reduce the minimum detectable velocity for Moving Target Indicator (MTI) radars. Basically, sidelooking arrays only have one clutter notch because of the range independence of the main beam. In contrast, forward looking arrays can have multiple clutter notches from ambiguous clutter as a result of the range dependency. The multiple clutter notches may only appear for ranges less than 5 times the altitude as reported in [1].

Figure 4.8 shows two clutter notches for the forward looking case at a range of 12 km using output Signal-to-Interference-plus-Noise Ratio (SINR) analysis. The first notch is due to the unambiguous range ring while the second visible notch is due to the ambiguous clutter. There are actually two ambiguous range rings but the Doppler frequency from these two ranges is approximately the same. This far range effect occurs because the term $\cos(\theta)$ in Eqn. (4.2) does not vary much at far ranges. Figure 4.9 illustrates that the range dependency effects are minimized at ranges greater than 5 times the altitude for forward looking arrays. There is only one clutter notch and the optimum SINR is reached in the passband for a range

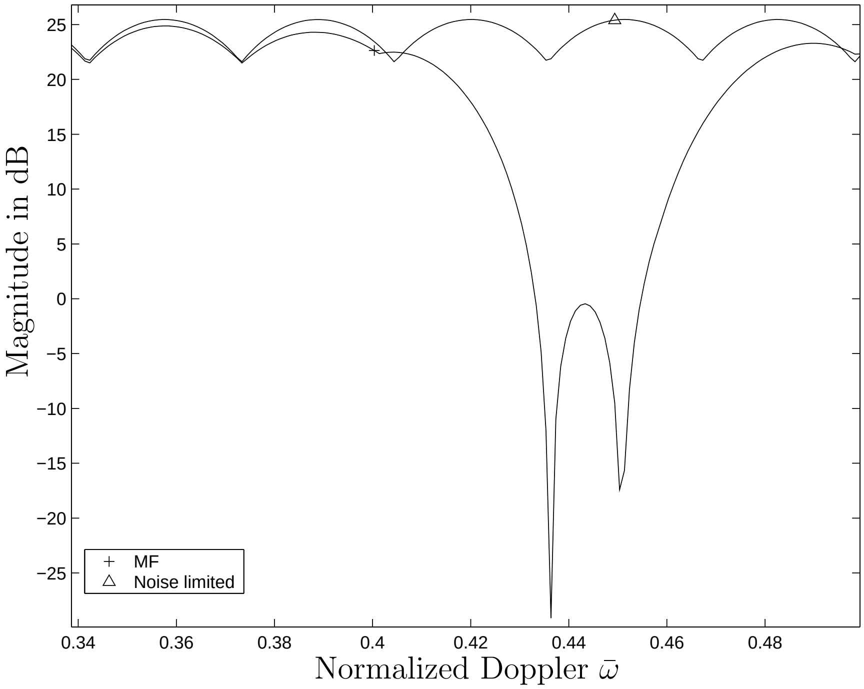

Figure 4.8: Multiple clutter notches for the forward looking array case. The range ambiguous clutter in the forward looking case causes multiple clutter notches.

of 66 km. The clutter notch is located at the frequency due to the aircraft motion and the θ corresponding to the range still though. In contrast, the clutter notch for sidelooking arrays is always at 0 Hz regardless of the range and there is always only one clutter notch. This effect is illustrated in Fig. 4.10.

4.6 Decorrelation Effects

Decorrelation effects result in increased clutter rank in the clutter covariance matrix. STAP works by finding statistical correlations in the interference returns but decorrelation effects increase the interference suppression problem difficulty by increasing the clutter rank. The increased clutter rank means wider clutter notches and more Degrees of Freedom (DOF) may be required to suppress the interference. The forward looking array case clutter environment is very severe and as a result decorrelation parameters affect results dramatically as shown in Fig. 4.11. One of

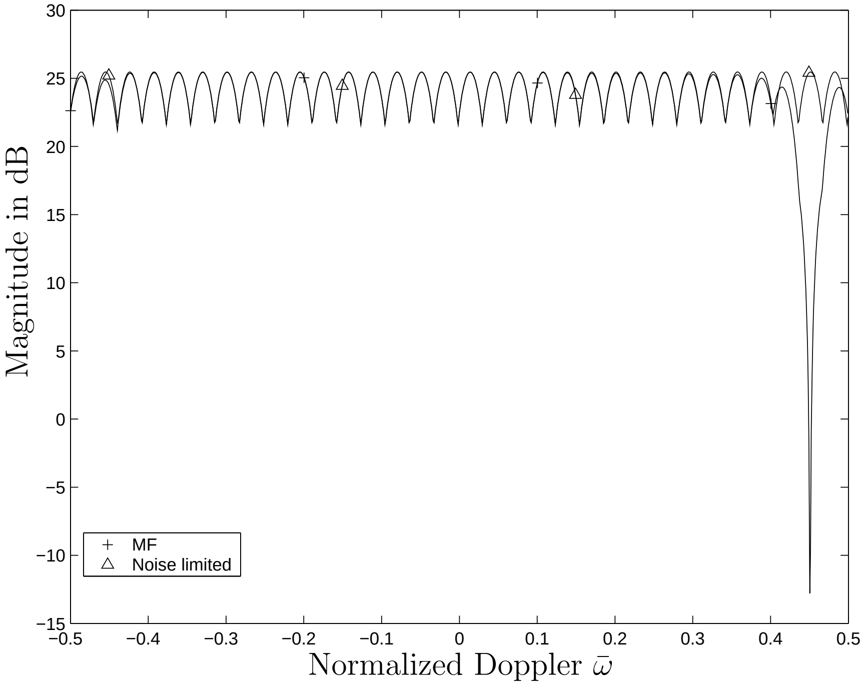

Figure 4.9: Single clutter notch for the forward looking array case at far range. As the range increases far enough out the ambiguous clutter is so far out that the range ambiguous clutter does not create noticeable multiple clutter notches

the reasons decorrelation parameters affect the forward looking case so dramatically is the multiple clutter notches spread out and there appears to only be one large clutter notch.

Decorrelation effects result in an increased clutter notch in the sidelooking case as well but not as dramatically as in the forward looking array case as shown in Fig. 4.12. The sidelooking array case can still reach the optimum SINR while the forward looking array case cannot reach the optimum SINR with added decorrelation effects. Figures 4.11 and 4.12 show the decreased performance due to decorrelation effects by illustrating the decreased output SINR.

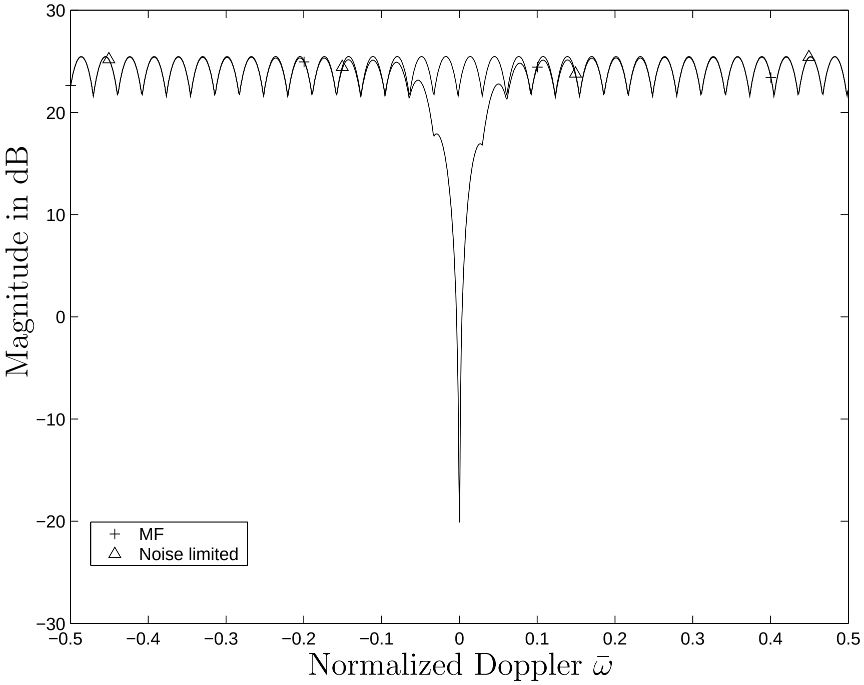

Figure 4.10: Single clutter notch for the sidelooking array case. The clutter notch for sidelooking radar is always at 0 Hz showing the range independence for main beam returns.

4.7 Summary

This chapter compares and contrasts the forward and sidelooking array cases. First, the differences in range cell homogeneity between the two array orientations are discussed and naturally lead into the different clutter ridge shapes and clutter covariance matrix ranks using eigenvalue analysis. The differences in the number of clutter nulls also directly result from the differences in range dependency between the forward and sidelooking array cases. Finally, Section 4.6 shows the increased difficulty involved in interference suppression when decorrelation parameters are added to the forward and sidelooking array cases. Since the differences between the two array orientations have been explained, the next step is to start applying STAP in the forward looking case in Chapter V for linear arrays.

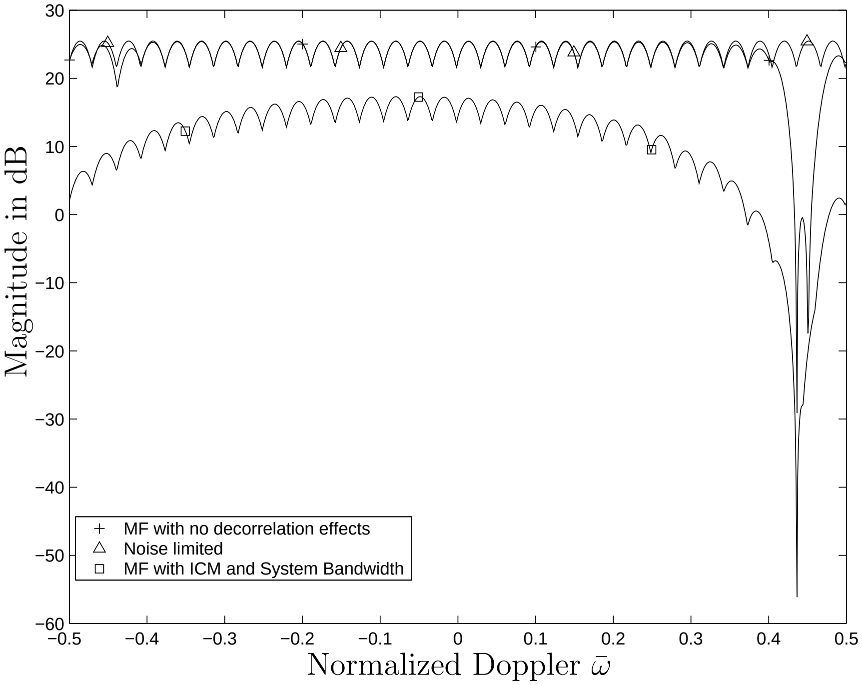

Figure 4.11: Decorrelation Effects for a forward looking array shown using output SINR. Notice the two clutter nulls from Fig. 4.8 blend together as a result of decorrelation parameters.

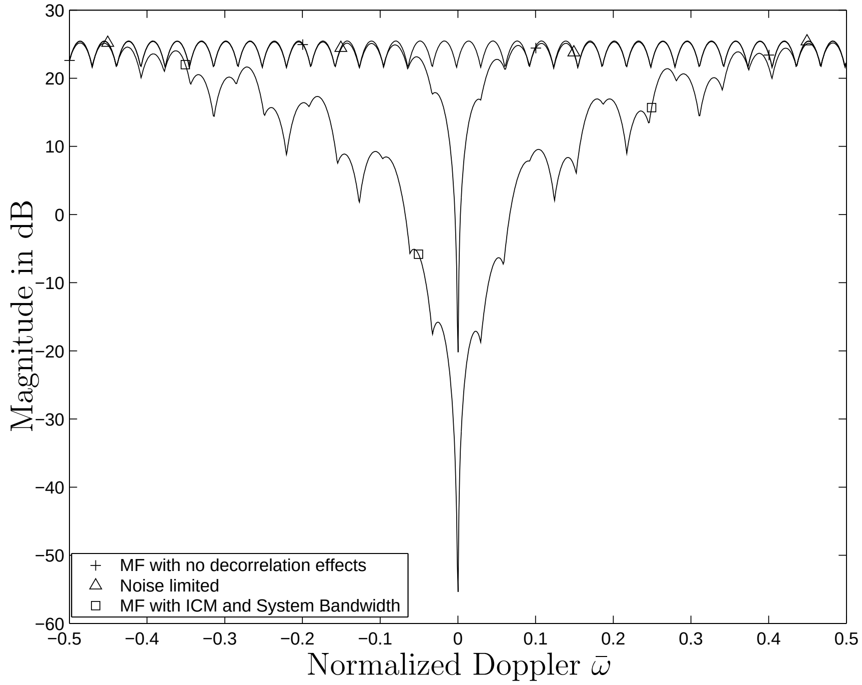

Figure 4.12: Decorrelation Effects for a sidelooking array shown using output SINR. Notice the widened clutter notch from Fig. 4.10 as a result of the added decorrelation parameters.

V. Interference Suppression in Forward Looking Linear Arrays

This chapter applies Space-Time Adaptive Processing (STAP) to forward looking linear arrays using adaptive interference suppression based on the data model introduced in Chapter III and the characteristics presented in Chapter IV. The goals include narrowing the combined clutter notch widened from the decorrelation effects and suppressing barrage noise jammer signals so target detection can improve for slow moving targets. Additionally, another benchmark for success is how close the partially adaptive STAP techniques approach the optimum output Signal-to-Interference-plus-Noise Ratio (SINR).

First, output SINR curves and antenna patterns using the Fourier Transform evaluate performance with an added barrage noise jammer to the covariance matrix. Then, Monte Carlo analysis predicts target detection probability for the STAP algorithms. Due to the harsh forward looking array environment, Section 5.4 offers an approach to change the Pulse Repetition Frequency (PRF) to improve results. Because of the harsh interference environment and need for further improvement, Chapter VI analyzes interference suppression using a planar array and notes the performance improvements.

Chapter V shows the result of adding a barrage noise jammer to the environment. The radar must adaptively suppress the added jamming spatially in addition to the harsh forward looking case clutter returns. Table 5.1 lists the jammer parameters but all other parameters remain the same from Table 4.1.

5.1 Output SINR

Output SINR is a useful performance metric because maximizing SINR is equivalent to maximizing detection probability [5]. The output SINR is defined as

$$\mathrm{SINR} = \frac{\sigma^2 \xi_t |\mathbf{w}^H \mathbf{v}_t|^2}{\mathbf{w^H R w}}, \tag{5.1}$$

Table 5.1: Jammer parameters.

Variable	Value
S_j	20 dBm/Hz
R_j	50 km
L_r	1
G_e	4 dB
B	800 kHz
f_o	1240 MHz
Element Pattern	Cosine
Element Backlobe Level	-15 dB
Transmit Taper	Uniform (None)
Jammer ϕ	45°
Jammer θ	0°

where ξ_t is the target signal to noise ratio and $\mathbf{v}_t$ is the target steering vector from Eqn. (2.11) [2]. SINR curves in this thesis are under known covariance and show Doppler straddling losses occurring when a target is in between two different Doppler filters.

Figure 5.1 shows output SINR curves for a forward looking array operating under the scenario conditions in Tables 4.1 and 5.1. Figure 5.1 shows output SINR curves for the Matched Filter (MF), Joint Domain Localized (JDL), Parametric Adaptive Matched Filter (PAMF), Factored Time-Space (FTS), Signal Match (SM), and Noise limited cases.

The figure clearly indicates a *clutter limited* detection scenario. The thermal noise upper bound is significantly above the output SINR produced by the conventional processing method SM, indicated by the curve with the square marker. The Noise limited bound represents radar performance with *no clutter*. Hence, it is not directly comparable to the other curves in the figure. It's presence within the figure illustrates clutter impact on output SINR.

As expected when using a forward looking radar, a sharp dip in output SINR occurs at a normalized Doppler corresponding to mainbeam clutter [25]. In this

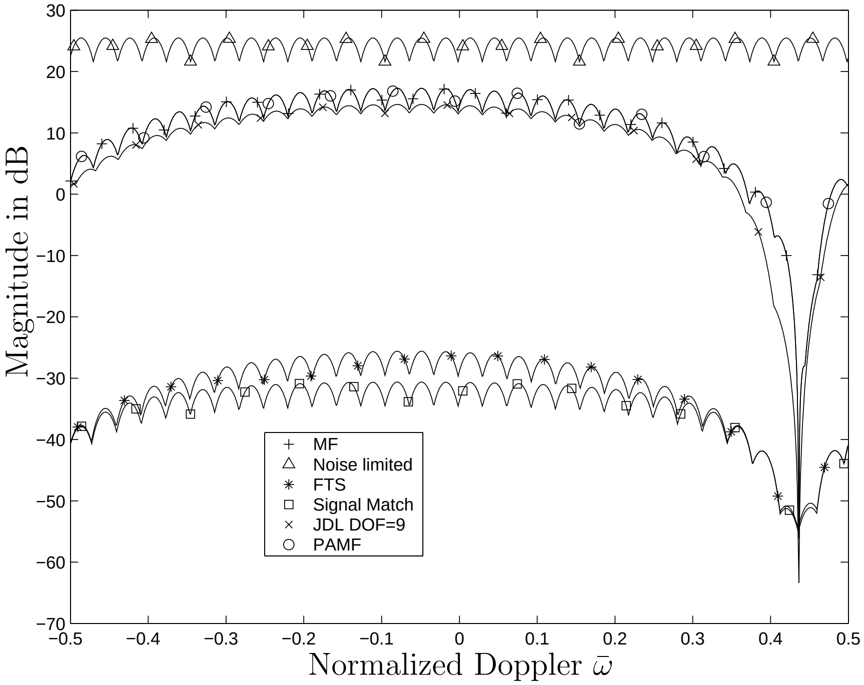

Figure 5.1: Output SINRs curve with a barrage noise jammer. Notice the MF does not reach the Noise limited curve due to the harsh clutter limited environment.

scenario, the performance drop occurs at $\bar{\omega} \approx 0.43$. Internal Clutter Motion (ICM) effects cause broadening of this "null" while System Bandwidth effects reduce the overall performance across the entire normalized doppler spectrum. The output SINR "null" occurs because the target resides in a physical location identical to mainbeam clutter. There is no domain available to the radar, either azimuth or doppler, where the target can be separated from this mainbeam clutter. Subsequently, performance drops.

The MF represents an upper performance bound within the clutter limited scenario. As shown in [12], the MF provides maximum output SINR given known interference statistics. The figure illustrates each STAP method obeys this result. The MF results also indicate an environment with strong clutter infiltration since the MF curve remains approximately 10 dB below the Noise limited detection scenario.

Of interest is FTS's inability to significantly improve output SINR. This result is expected since FTS is a post-doppler method where adaptivity is only performed within azimuth. A conventional doppler filter bank is used before azimuth adaptivity. Given this insight, the method is not truly STAP since it is not adaptive within two dimensions. The clutter environment simply overwhelms the approach and performance suffers.

The other STAP techniques offer excellent performance within this forward looking scenario. The JDL approach is implemented with a small 3×3 Localized Processing Region (LPR), resulting in 9 DOF. However, by operating within a domain where the target is localized to a single bin, a large adaptivity region is not required as shown by the performance results. Sample support requirements remain conservative because of the small DOF used. These requirements obey Reed's Rule of twice the DOF, meaning only 18 space-time snapshots, e.g., 18 range cells of data, were required for interference statistics estimation. Performance is within 3 dB of the MF.

The PAMF using known interference statistics, as in this output SINR analysis, is mathematically equivalent to the MF. The figure clearly indicates this result holds within the simulation since both curves lie directly on top of each other. The true advantage of the PAMF is shown in the detection probability analysis, where interference statistics or filter coefficients must be estimated from available data.

5.2 Antenna Beam Patterns

The antenna beam pattern is a useful performance metric because one can see what effect the STAP algorithm is having on the array pattern. The Fourier transform is used to obtain this beam pattern because of the equivalence of the steering vector to the Fourier transform as shown below [10]. The Discrete Fourier

Transform (DFT) is defined as [26]

$$W[k] = \sum_{n=0}^{N-1} w[n] e^{-j2\pi kn/N}. \tag{5.2}$$

Substitute into Eqn. (5.2) the azimuth steering vector from Eqn. (3.21) to get

$$W[k] = \sum_{n=0}^{N-1} a^*[n] w[n] = \sum_{n=0}^{N-1} w[n] e^{-j2\pi n d_x cos(\theta) sin(\phi_k)/\lambda_o}, \tag{5.3}$$

where k from Eqn. (5.2) equals $\frac{N d_x cos(\theta) sin(\phi_k}{\lambda_o}$. After a DFT shift and using the linspace command in Matlab®, the azimuth axis scale becomes

$$\phi = \sin^{-1}\left[\frac{\lambda_o}{2d_x}\text{linspace}(-1, 1-1/N, N)\right]. \tag{5.4}$$

The equivalence of the azimuth steering vector to the DFT has been shown and in the same way the space-time steering vector is equivalent to the multi-dimensional DFT.

The optimum beam pattern should place nulls across the clutter ridge and null the jammer. In addition, it should have a peak response where the radar is looking for a target. In this case, the radar is looking for a target with a normalized Doppler of 0.25 at 0° azimuth and 0° elevation. Figure 5.2 shows the beam pattern for the MF. The MF beam pattern clearly nulls the clutter ridge and the jammer located at 45° in azimuth. Both SM and FTS are not adaptive in Doppler and thus cannot null out the clutter ridge. FTS does have a null close to 45° in azimuth though and this helps to explain why FTS has slightly better performance than SM in Fig. 5.1. The beam pattern for FTS and SM are shown in Figs. 5.3 and 5.4 respectively. JDL places a null at 45° in azimuth but only in the Localized Processing Region (LPR) and also places peak response where the radar is looking for a target. This beam response, shown in Fig. 5.5, obtains output SINR close to the MF's response with

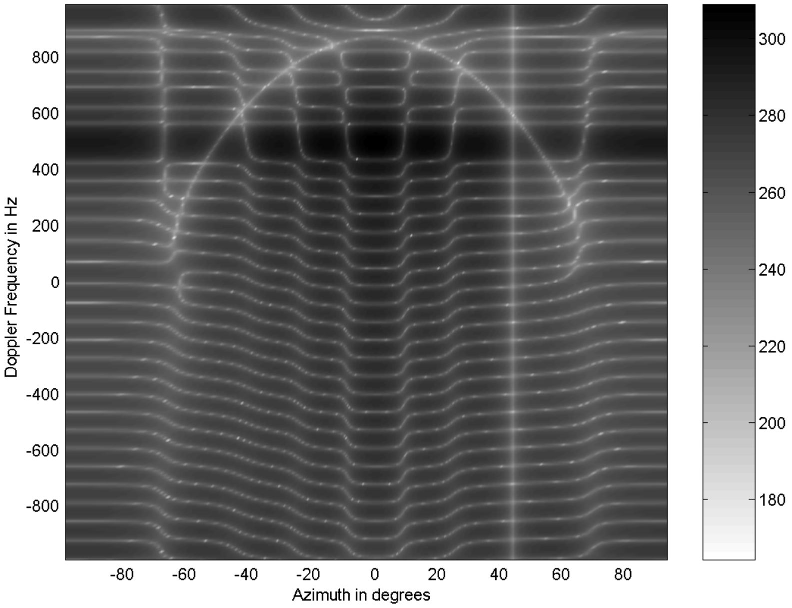

Figure 5.2: Antenna beam pattern for the MF with a noise jammer. Notice the MF places nulls along the clutter ridge and the jammer.

far fewer DOF's. Under known covariance, the PAMF Auto-Regressive (AR) filter coefficients are known [14]. As a result, the PAMF beam pattern nulls the clutter ridge and the jammer while placing peak response where the radar is looking for a target as shown in Fig. 5.6.

5.3 Detection Probability

Monte Carlo analysis predicts detection probability based on threshold crossings for a fixed false alarm rate. All detection curves correspond to 0.01 false alarm probability (P_{fa}) and $1,000$ trials. The number of trials used in Monte Carlo analysis is $10/P_{fa}$ [19]. A magnitude squared test statistic is used to provide data for thresholding, where the threshold is determined from the desired P_{fa} and $\boldsymbol{\chi}$ with no target present. Clearly, data for detection uses $\boldsymbol{\chi}$ with a target present at specified SINR values.

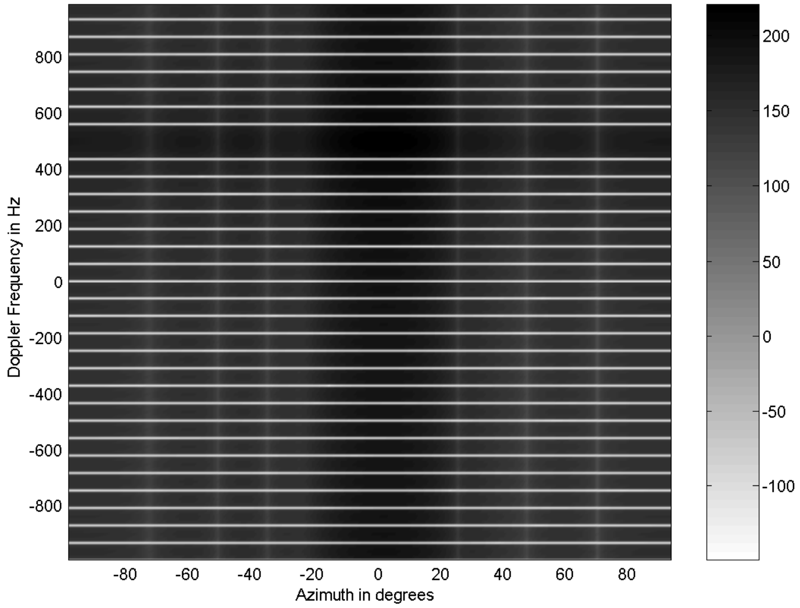

Figure 5.3: Antenna beam pattern for FTS with a noise jammer. Notice the lack of Doppler adaptivity means FTS is unable to place nulls along the clutter ridge.

Monte Carlo simulations model detection probability curves for radars under estimated interference statistics. The traditional STAP methods use twice the DOF independent and identically distributed (iid) space-time snapshots for covariance matrix estimation. This rule of thumb is called Reed's Rule, shown mathematically to provide average performance within 3 dB of the known covariance output SINR [5, 16]. Hence, FTS requires $2N = 22$ snapshots, the Adaptive Matched Filter (AMF) requires $2NM = 704$ snapshots, and JDL requires twice the product of the LPR dimensions or 18 snapshots.

The disadvantage of fully adaptive methods becomes immediately clear. The AMF requires 704 sample support range cells, much larger than the typical number available. The radar under consideration only has $1/T_p f_r = 630$ range cells available. For the purposes of this simulation, a full 704 samples were generated although they clearly result in AMF performance much better than can be expected in real world application. The AMF method *does* offer a performance benchmark and this reason

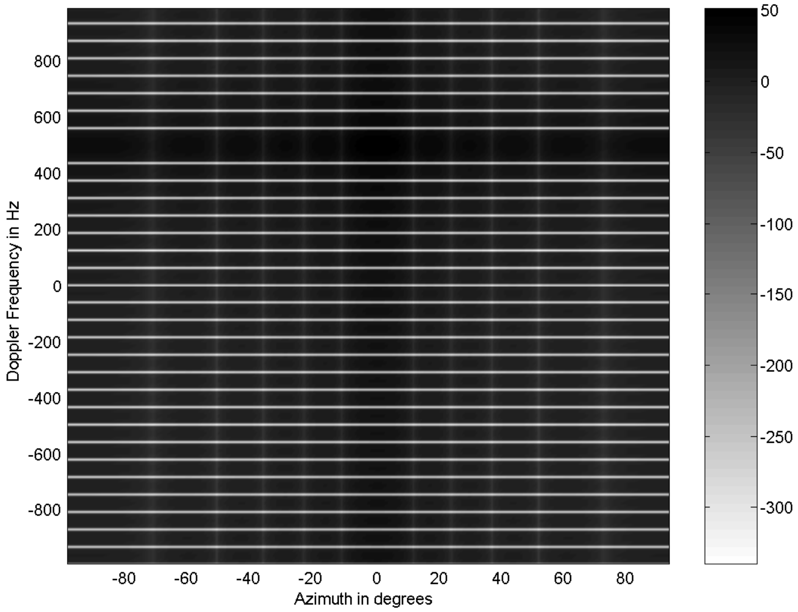

Figure 5.4: Antenna beam pattern for SM with a noise jammer. Notice the similarities between SM and FTS in Fig. 5.3.

is why it's included in these results. For comparison, only 8 snapshots were used to estimate the AR filter coefficients within the PAMF.

Sample support is a critical issue within adaptive interference suppression. For sidelooking radar, the clutter structure does not change with range cells, although it's amplitude does suffer range attenuation effects. Using this fact, range cells serve as a dimension where the data is approximately homogeneous and *approximately* iid samples are available. Real world effects sometimes destroy this homogeneity when considering large regions as required in the AMF. However, the assumption still holds for small regions corresponding to the sample support required for partially adaptive methods. Based on these observations, the iid assumption works well for partially adaptive interference suppression techniques applied to sidelooking radar and range is a suitable dimension for drawing iid samples.

This iid assumption does not hold for forward looking radar. As previously discussed in Chapter IV, clutter structure changes on a range cell basis. For this

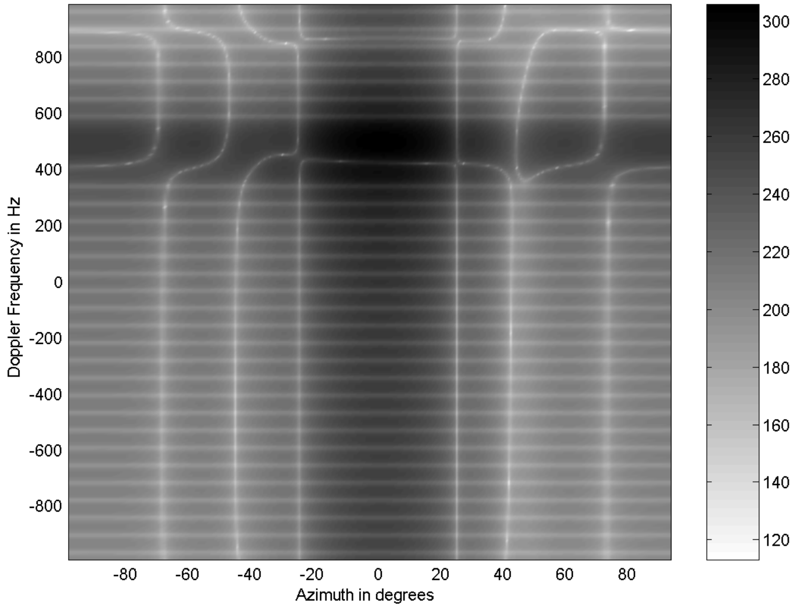

Figure 5.5: Antenna beam pattern for JDL with 9 DOF and a noise jammer. Notice JDL is only adaptive within its LPR.

reason, extremely small sample support requirements are needed. Such requirements allow applying the iid assumption across a very small range extent where it might apply in an approximate sense. Within this context, the extremely small footprint represented by the PAMF is highly desirable.

Data in this section is generated using two different approaches. First, Fig. 5.7 offers detection analysis when the actual data is generated as iid, but the clutter shape corresponds to a forward looking radar at the specified target range. Generating data in this manner relieves the computational load involved in the simulation since a single covariance matrix, corresponding to the specified target range and forward looking radar, is used to color white data. This analysis provides information on how well the different techniques handle the different clutter structure, as opposed to published results on sidelooking radar.

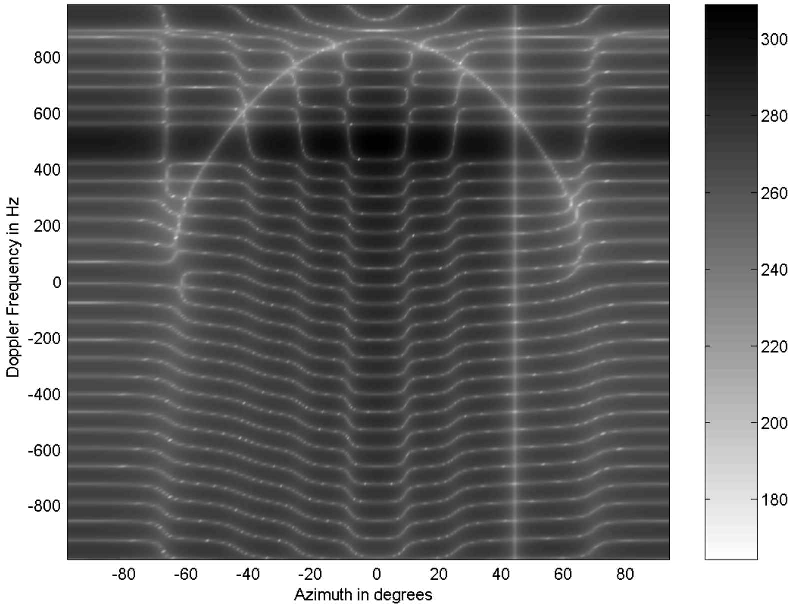

Figure 5.6: Antenna beam pattern for the PAMF with a noise jammer. Notice the PAMF places nulls along the clutter ridge and the jammer.

Figure 5.7 shows detection probability versus *input* SINR on a per element, per pulse basis. Since the interference environment is now estimated, the MF curve is no longer used and replaced by the AMF.

Discussion focuses on the PAMF since the other curves generally mirror their counterparts within the output SINR analysis. Note FTS actually performs worse than conventional processing techniques, a result not predicted by the output SINR curves. This performance degradation occurs because, under known covariance in Fig. 5.1, FTS was barely performing better than SM. According to Reed's Rule there is a drop in performance when estimating the covariance matrix. Since SM does not estimate interference statistics, it does not suffer this loss and subsequently outperforms FTS in this scenario [25]. Noticing when conventional methods like SM actually outperform FTS is an important point since there are some scenarios when traditional radar processing is adequate and adaptive methods are not needed.

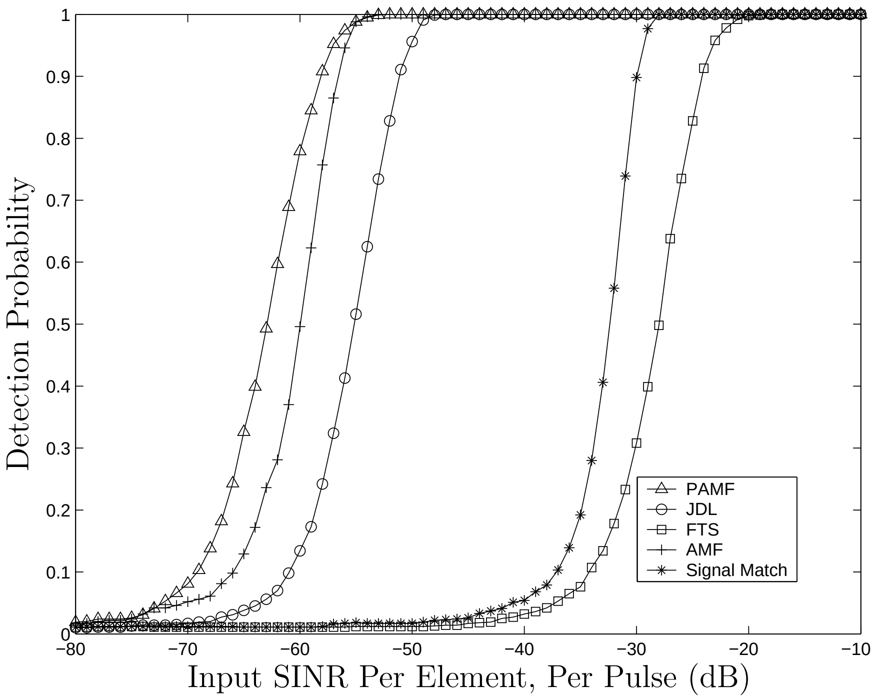

Figure 5.7: Monte Carlo analysis shows P_d curves for $1,000$ trials with P_{fa} of 0.01 for a forward looking array using iid generated data.

The sample support advantage of the PAMF becomes clear from Fig. 5.7. The method offers much better performance than any other method, with the smallest sample support. Requiring such a small number of space-time snapshots for AR filter coefficient estimation makes the method much less susceptible to inconsistencies within the data.

The second data generation approach uses the correct covariance matrix for *each* range cell within the sample support of the specified techniques [27]. Correspondingly, this approach is a very computationally intensive simulation but does provide results *faithfully representing true forward looking radar performance*. Furthermore, comparison between this method and the results of Fig. 5.7 allow determining the heterogeneous data impact as shown in Fig. 5.8 for the PAMF, JDL, and FTS. SM processing is not included because it does not change for either approach since no sample support is used. AMF is not compared since it is not physically realizable because there are only 630 range cells available and AMF requires 704. The results corresponding to iid generation use the solid lines and the results corresponding to the second data generation approach use dash-dot lines. The STAP algorithms all suffer a performance hit because the data is no longer iid. Even though the AMF was not simulated, the reader can clearly imagine the AMF performance degradation would be greater because of the even larger number of sample support used. FTS suffers the largest performance hit in Fig. 5.8 because it uses the largest number of sample support, 22. Even though PAMF uses less sample support than JDL, JDL suffers less of a heterogeneity loss than PAMF. A reason for this discrepancy may be explained by the differences in approach between the two methods. PAMF uses an AR model while JDL uses a beamspace approach. The PAMF with only 8 sample support cells still outperforms JDL with 18 sample support in Fig. 5.8. The PAMF and JDL processing techniques perform the best with regards to detection probability of the algorithms considered in Chapter V.

Due to the harsh forward looking environment, less sample support meets the iid assumption compared to the sidelooking array case. As a result, STAP algorithms experience a loss when used in the forward looking case as compared to the sidelooking case. Figure 5.9 illustrates this detection loss for the PAMF and JDL processing techniques. The sidelooking case data uses solid lines and the forward looking data that accounts for heterogeneities uses dash-dot lines. This detection loss is the price aircraft pay for operating in the forward looking environment.

5.4 Changing the Pulse Repetition Frequency

STAP for linear arrays does offer tremendous improvement over the SM processing approach as shown in 5.1 but the ambiguous clutter returns are not attenuated. The lack of attenuation occurs because two-dimensional STAP is not capable of nulling ambiguous clutter. Therefore, Wang, Bao, and Peng suggest using multiple PRFs to get better performance results in STAP for forward looking radar

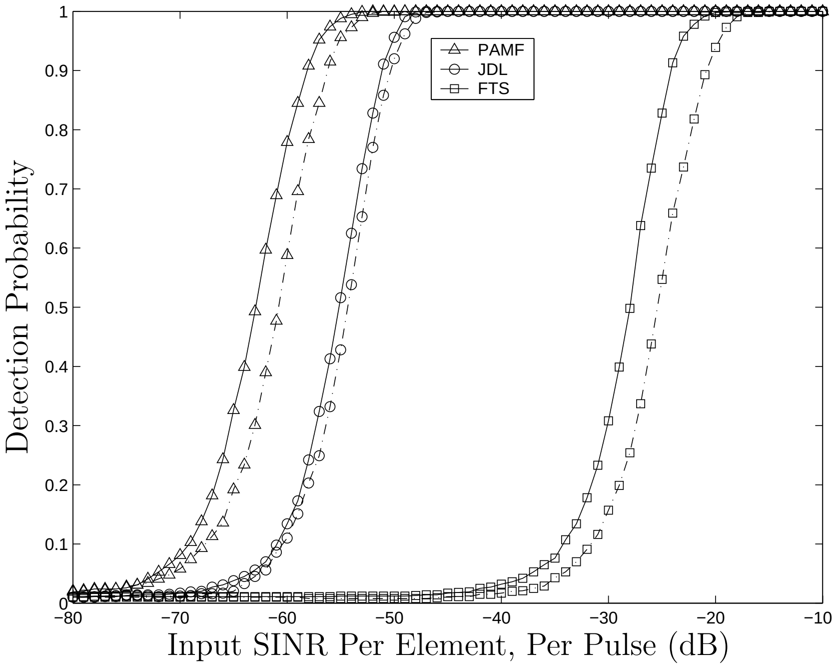

Figure 5.8: Monte Carlo analysis shows P_d curves for $1,000$ trials with P_{fa} of 0.01 comparing the two different data generation approaches. The iid generation approach uses solid lines and the heterogeneity approach uses dash-dot lines.

results [28]. Changing the PRF means the target may change locations with regards to the clutter ridge in the Doppler space. If the target is no longer obscured by the clutter in the Doppler bin, then target detection is improved. However, if the PRF is decreased too much, then Doppler ambiguities occur instead of the range ambiguities. Doppler ambiguities are particularly to be avoided though in the forward looking array case.

5.5 Summary

This chapter uses STAP on forward looking linear arrays for interference suppression and increased target detection. Output SINR results for STAP techniques show tremendous improvement over traditional SM processing. However, two-dimensional (2D) STAP is not capable of reaching the passband for the forward looking

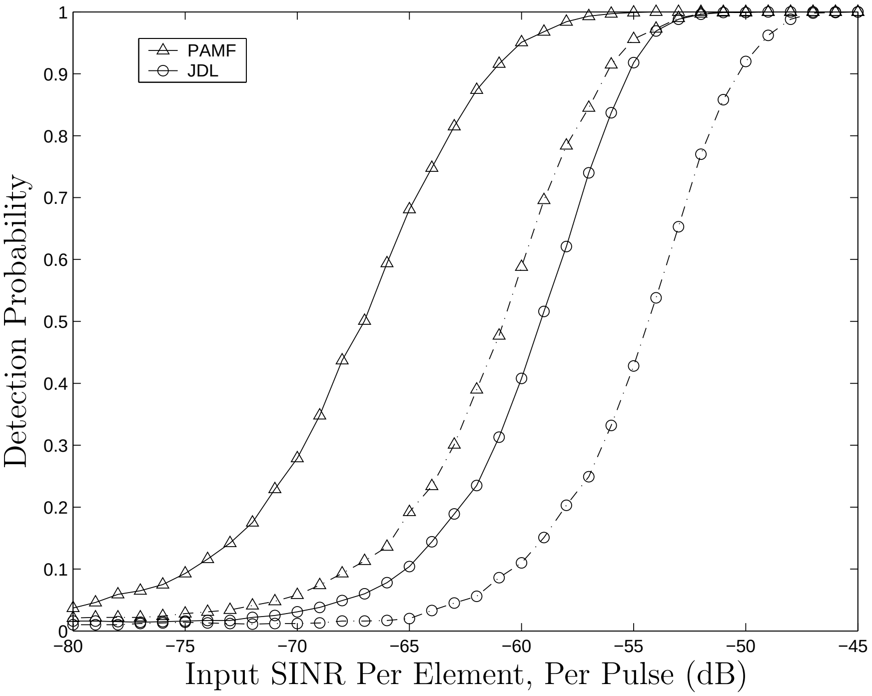

Figure 5.9: Monte Carlo analysis shows P_d curves for $1,000$ trials with P_{fa} of 0.01 comparing the sidelooking array case with the forward looking array case. The sidelooking case data uses solid lines and the forward looking data that accounts for heterogeneities uses dash-dot lines.

case even with the MF and the clutter notch is still large enough to degrade slow moving target detection.

Detection probability curves in general track the output SINR curves with two exceptions. FTS performance degrades below SM performance because of the loss associated with estimating the covariance matrix and PAMF performance exceeds AMF target detection rates. The PAMF and JDL algorithms perform the best out of the implementable techniques used in Chapter V.

Because of the wide clutter notch, an approach has been proposed to change the PRF so the target may no longer have to compete with the clutter in the Doppler space. Unfortunately, changing the PRF may cause Doppler ambiguities while trying to eliminate range ambiguities. Therefore, three-dimensional (3D) STAP is needed to null the range ambiguous clutter while not causing Doppler ambiguities as discussed in Chapter VI.

VI. Interference Suppression In Forward Looking Planar Arrays

As discussed in Chapter V, Space-Time Adaptive Processing (STAP) for linear arrays is not capable of obtaining the output Signal-to-Interference-plus-Noise Ratio (SINR) results needed for detecting slow moving targets near the mainbeam clutter and nulling range ambiguous clutter. Therefore, three-dimensional (3D) STAP is used to attenuate the range ambiguous clutter and narrow the clutter notch by adding elevation adaptivity. This chapter fulfills the ultimate goal in STAP by successfully attenuating range ambiguous clutter using 3D adaptivity.

Section 6.1 gives the simulation parameters used in Chapter VI and shows the narrowed clutter null and improved pass band results using output SINR analysis. Then, Section 6.2 shows SINR Loss analysis to show the improved results by comparing two-dimensional (2D) STAP to 3D STAP. The final sections show detection probability and maximum detection range analysis for 3D STAP.

6.1 3D STAP

Table 6.1 shows the parameters used in this chapter. All of the parameters are constant from Table 4.1 except for P, the number of elevation elements, which changes from 1 to 3. The additional elevation elements allow the cancellation of range ambiguous clutter without having to change the Pulse Repetition Frequency (PRF). This added adaptivity means 3D STAP can improve slow target detection without causing Doppler ambiguities that might degrade faster moving target detection. Note the Parametric Adaptive Matched Filter (PAMF) is not included in Chapter VI because it has not been extended to planar arrays.

Figure 6.1 shows the narrowed clutter notch and the improved passband output SINR for 3D STAP. The Matched Filter (MF) actually reaches the Noise Limited SINR value in the passband and the Joint Domain Localized (JDL) closely approximates the MF curve with only 27 Degrees of Freedom (DOF). Factored Time-Space

Table 6.1: Scenario parameters.

Variable	Value
M	32
N	11
P (only change)	**3**
f_o	1240 MHz
f_r	1984 Hz
T_p	0.8 μs
P_t	200 kW
B	800 kHz
F_n (Noise Figure)	3 dB
N_c	361
h_a (aircraft altitude)	3073 m
v_a (aircraft velocity)	$\frac{d_x f_r}{2}$
R	12 km
γ	-3 dB
Array Transmit Gain	22 dB
Element Pattern	Cosine
Element Gain	4 dB
Element Backlobe Level	-40 dB
d_x	0.10922 m
d_z	0.1407 m
Transmit Taper	Uniform (None)
System Losses L_s	3 dB
Target ϕ	0°
Target θ	0°
Target $\bar{\omega}$	0.25
B_c	$\frac{10}{f_r}$
S_j	20 dBm/Hz
R_j	50 km
L_r	1
G_e	4 dB
Jammer Element Backlobe Level	-15 dB
Jammer ϕ	45°
Jammer θ	0°
ξ_t	1

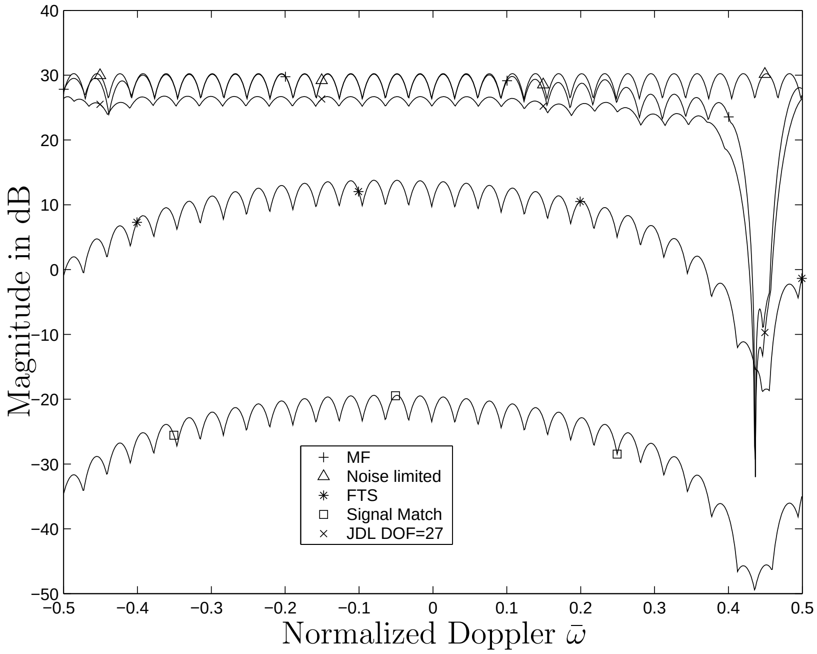

Figure 6.1: Output SINR for a forward looking planar array. Notice the narrowed clutter notch compared to Fig. 5.1.

(FTS) shows tremendous improvement over the output SINR curve from Fig. 5.1. In Fig. 5.1, the FTS curve is only slightly better than the Signal Match (SM) curve. By adding elevation adaptivity, FTS has an output SINR curve almost 30 dB higher than SM! In addition, elevation adaptivity has significantly narrowed the clutter notch so slow moving target detection is improved. The decorrelation effects cause a widening of the clutter notch that 2D STAP is incapable of compensating for. In contrast, 3D STAP with elevation adaptivity is able to significantly narrow the clutter notch.

6.2 SINR Loss

SINR Loss is a performance metric indicating how closely a processing technique approaches the coherent integration processing gain (the best an algorithm can do). This section uses SINR Loss for comparing STAP for linear arrays versus STAP for planar arrays. The reason SINR Loss is used is because by adding elevation

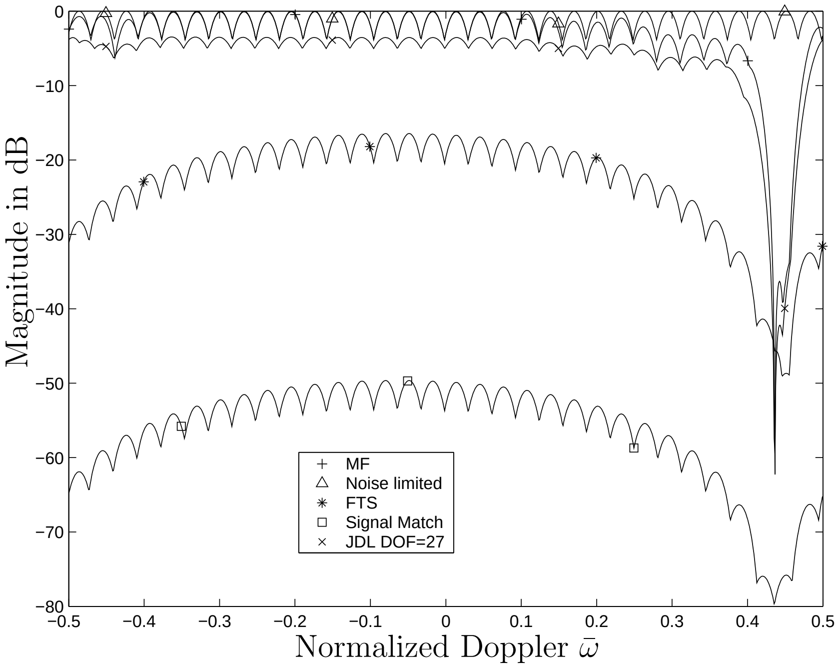

Figure 6.2: SINR Loss for a forward looking planar array. Notice the narrowed clutter notch compared to Fig. 6.3.

elements, more DOF have been added. Since the product MNP is higher for planar arrays, the output SINR curves are higher for the planar arrays. The reason the choice was made to increase the number of DOF, instead of reducing the number of azimuth elements to keep the number of DOF constant, is only one factor is changed by increasing P to 3. By keeping the number of DOF constant, the elevation and azimuth beam patterns are changed and this makes a comparison very difficult.

Therefore, SINR Loss is used to compare the 2D and 3D STAP results. SINR Loss is defined as the coherent integration gain, MNP, minus the output SINR for the processing techniques. The comparison is based on how closely the algorithm approaches the optimum coherent processing value. Figure 6.2 shows the SINR Loss curves for 3D STAP. In contrast, Fig. 6.3 shows the SINR loss curves for 2D STAP. The clutter notch is clearly narrower for planar arrays and there is actually no SINR

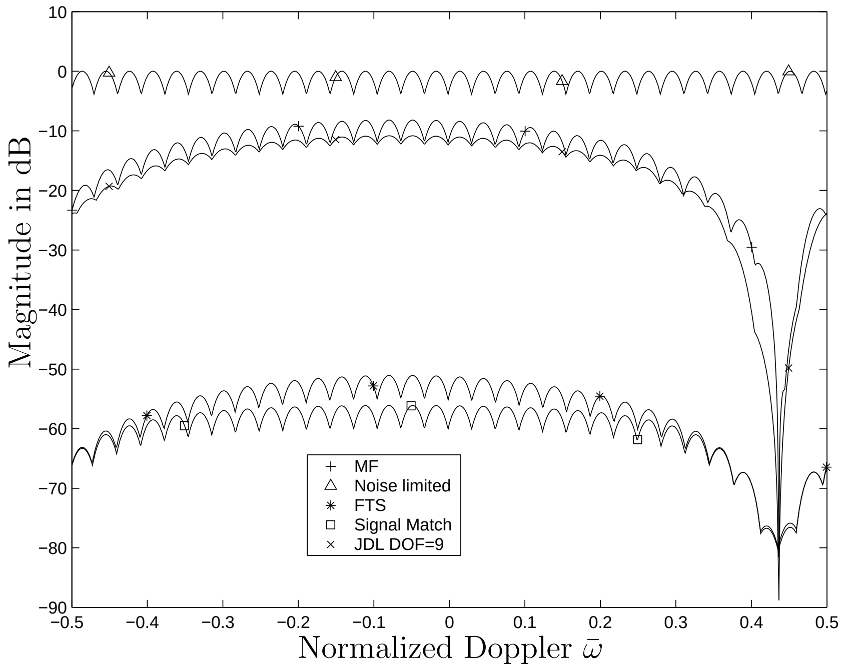

Figure 6.3: SINR Loss for a forward looking linear array.

loss in the passband for planar arrays whereas there is significant SINR loss for linear arrays.

Figure 6.4 shows the significantly better performance obtained by adding elevation adaptivity using SINR Loss curves for the MF with $P = 1$ and $P = 3$. The MF curve for $P = 3$ narrows the clutter notch and reaches the passband by nulling the range ambiguous clutter.

6.3 Detection Probability

As discussed in Chapter V, Monte Carlo analysis predicts detection probability based on threshold crossings for a fixed false alarm rate. All detection curves correspond to 0.01 false alarm probability (P_{fa}) and $1,000$ trials. The number of trials used in Monte Carlo analysis is $10/P_{fa}$ [19].

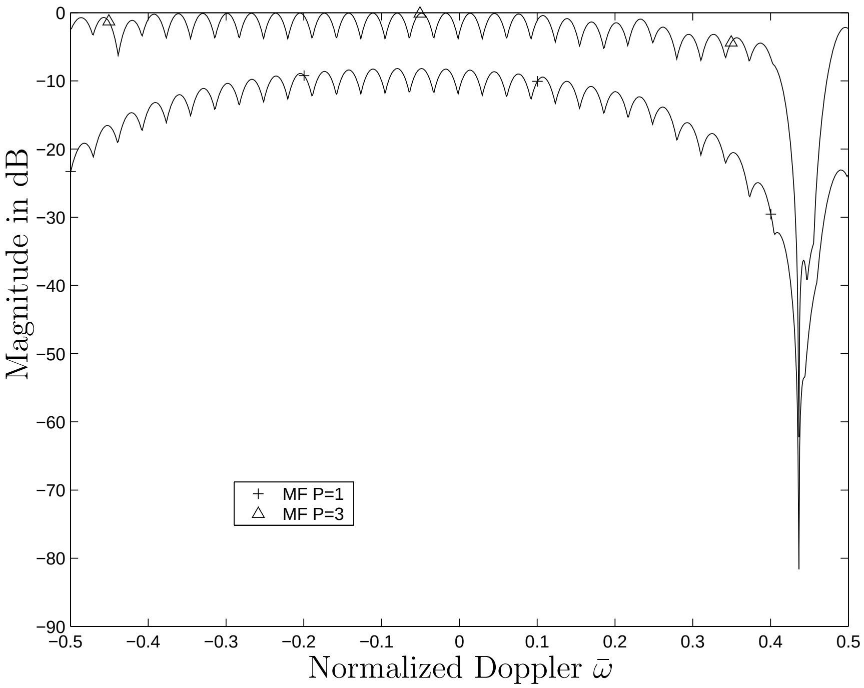

Figure 6.4: SINR Loss for the MF for forward looking linear and planar arrays. Notice the narrowed clutter notch and improved passband for the $P = 3$ MF curve.

Following Reed's Rule [12], FTS requires $2NP = 66$ snapshots, the Adaptive Matched Filter (AMF) requires $2MNP = 2112$ snapshots, and JDL requires twice the product of the Localized Processing Region (LPR) dimensions or 54 snapshots.

Once again, the disadvantage of fully adaptive methods becomes immediately clear. The AMF requires 2112 sample support range cells, much larger than the typical number available. The radar under consideration only has $1/T_p f_r = 630$ range cells available. For the purposes of this simulation, a full 2112 samples were generated although they clearly result in AMF performance much better than can be expected in real world application. The AMF method *does* offer a performance benchmark and this reason is why it's included in these results.

Sample support is a critical issue within adaptive interference suppression. The iid assumption does not hold for forward looking radar. As previously discussed in Chapter V, clutter structure changes on a range cell basis. For this reason, extremely small sample support requirements are needed. Such requirements allow applying the iid assumption across a very small range extent where it might apply in an approximate sense.

Data in this section is generated using the same two approaches from Chapter V. First, Fig. 6.5 offers detection analysis when the actual data is generated as iid, but the clutter shape corresponds to a forward looking radar at the specified target range. Figure 6.5 shows detection probability versus *input* SINR on a per element, per pulse basis. Since the interference environment is now estimated, the MF curve is no longer used and replaced by the AMF.

Note FTS actually performs much better than it did in Chapter V, because FTS is adaptive both in azimuth and elevation now whereas before it was only adaptive in azimuth for linear arrays.

The second data generation approach uses the correct covariance matrix for *each* range cell within the sample support of the specified techniques. Correspondingly, this approach is very computationally intensive but does provide results *faithfully representing true forward looking radar performance*. Furthermore, comparison between this method and the results of Fig. 6.5 allow determining the heterogeneous data impact as shown in Fig. 6.6 for JDL and FTS. SM processing is not included because it does not change for either approach since no sample support is used. AMF is not compared since it is not physically realizable because there are only 630 range cells available and AMF requires 2112. The results corresponding to iid generation use the solid lines and the results corresponding to the second data generation approach use dash-dot lines. The STAP algorithms both suffer a performance hit because the data is no longer iid. Even though the AMF was not simulated, the reader can clearly imagine that the AMF performance degradation would be greater because of the even larger number of sample support used. FTS suffers the largest performance hit in Fig. 6.6 because it uses the largest number of sample support, 66. The heterogeneity loss in JDL is noticeably smaller for both linear and planar

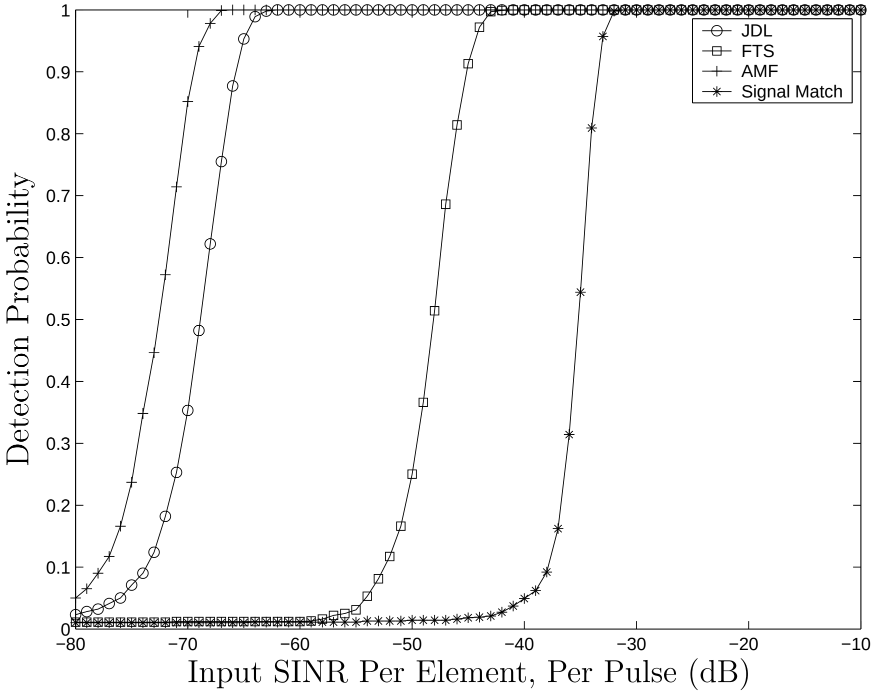

Figure 6.5: Monte Carlo analysis shows P_d curves for $1,000$ trials with P_{fa} of 0.01 for a forward looking array using iid generated data.

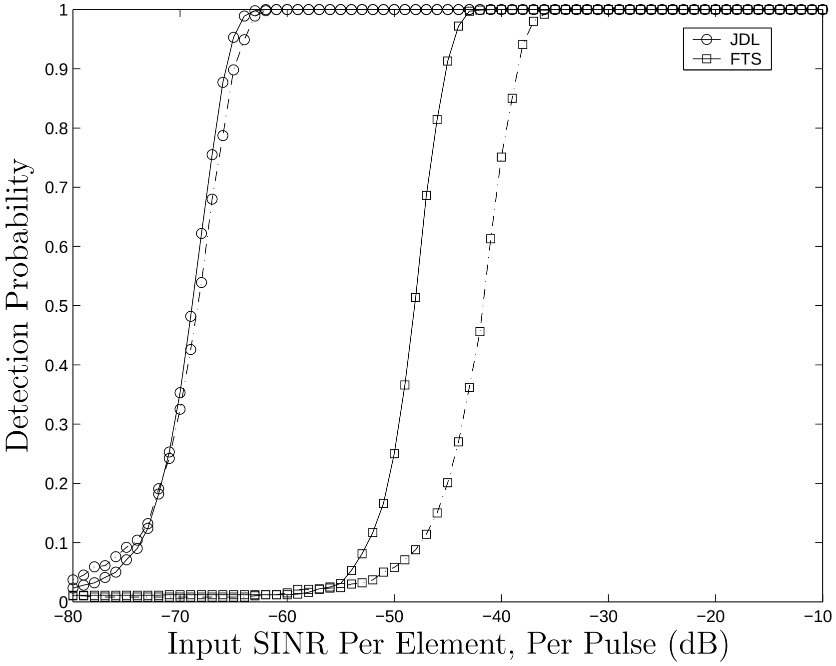

Figure 6.6: Monte Carlo analysis shows P_d curves for $1,000$ trials with P_{fa} of 0.01 comparing the two different data generation approaches. The iid generation approach uses solid lines and the heterogeneity approach uses dash-dot lines.

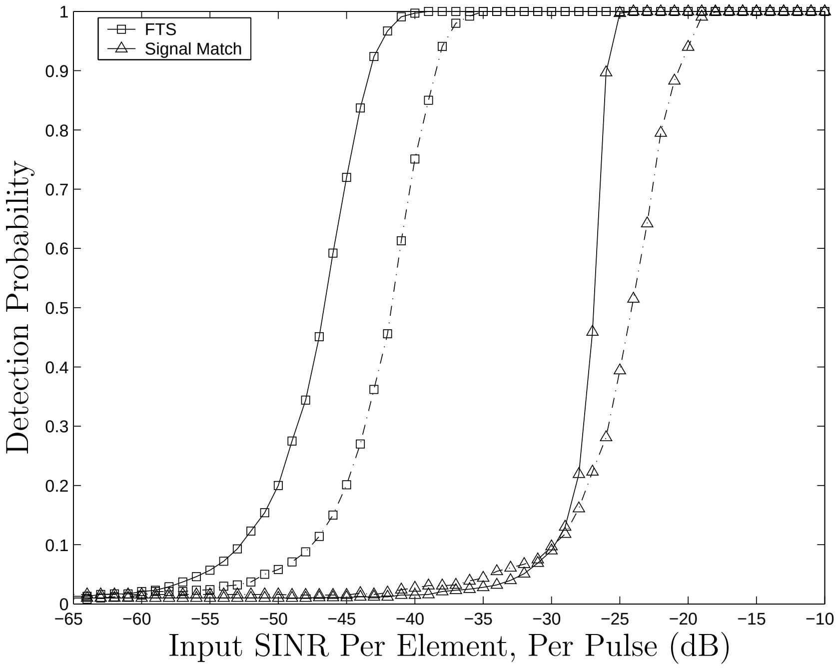

Figure 6.7: Monte Carlo analysis shows P_d curves for $1,000$ trials with P_{fa} of 0.01 comparing the sidelooking array case with the forward looking array case. The sidelooking case data uses solid lines and the forward looking data that accounts for heterogeneities uses dash-dot lines.

arrays than it is for FTS. This smaller loss can be explained because fewer DOF are used and JDL's LPR approach is more robust than the factored approach used in FTS.

Due to the harsh forward looking environment, less sample support meets the iid assumption compared to the sidelooking array case. As a result, STAP algorithms experience a loss when used in the forward looking case as compared to the sidelooking case. Figure 6.7 illustrates this detection loss for the FTS processing technique and SM. The sidelooking case data uses solid lines and the forward looking data that accounts for heterogeneities uses dash-dot lines. This detection loss is the price aircraft pay for operating in the forward looking environment.

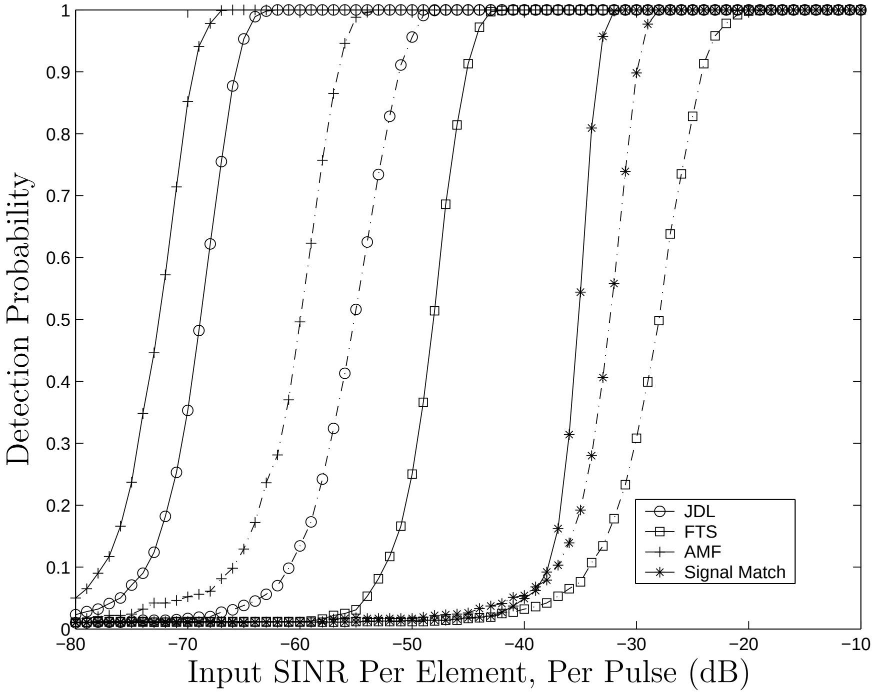

Figure 6.8: Monte Carlo analysis shows P_d curves for $1,000$ trials with P_{fa} of 0.01 comparing 3D STAP with 2D STAP using iid data. The 3D data uses solid lines and the 2D data uses dash-dot lines.

The ultimate comparison involves detection probability between 2D STAP and 3D STAP. Figure 6.8 compares forward looking radar detection probability rates for 2D and 3D STAP techniques using iid data. The 3D data is plotted using solid lines and 2D data with the dash-dot lines. Clearly, 3D STAP performs better than 2D STAP.

3D forward looking detection rates still exceed the 2D detection rates when the range heterogeneous data approach is used. Figure 6.9 compares the forward looking radar detection rates using data that accounts for range heterogeneities. The 3D data is plotted using solid lines and 2D data with dash-dot lines. Clearly, 3D STAP performs better than 2D STAP.

Looking at Fig. 6.9, several interesting facts can be observed. Both adaptive techniques, JDL and FTS, show improvement versus input SINR by going from

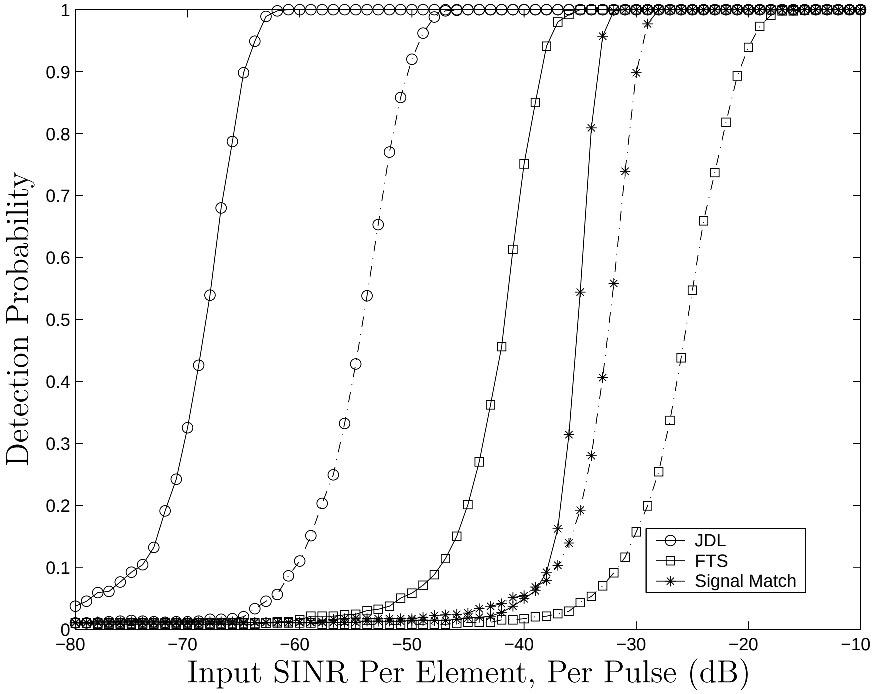

Figure 6.9: Monte Carlo analysis shows P_d curves for $1,000$ trials with P_{fa} of 0.01 comparing 3D STAP with 2D STAP using data that accounts for range heterogeneities. The 3D data uses solid lines and the 2D data uses dash-dot lines.

2D to 3D of approximately 13 dB and 16 dB respectively. Moreover, the detection probability versus input SINR curves improve over 30 dB comparing 3D JDL with the 2D conventional processing technique SM. These detection rate improvements show the value of 3D STAP and the need for elevation adaptivity in the range dependent forward looking case. As a result of the tremendous improvements in detection rates, the maximum detection range increases.

6.4 Maximum Detection Range Improvement

The theoretical maximum detectable range for a radar offers another point of comparison between the different STAP algorithms. The modified radar range

Table 6.2: Maximum Detection Range in km for the clutter limited forward looking scenario under consideration.

Algorithm	Linear Arrays	Planar Arrays
FTS	26.5	85.4
SM	45	63.6
JDL	144	392

equation from [6] gives the theoretical maximum detectable range as

$$R_{max} = \left(\frac{P_t G(\theta, \phi) g(\theta, \phi) \lambda^2 \sigma}{(4\pi)^3 \mathbf{R}(1,1) L_s \mathrm{SINR}_{\mathrm{in}}} \right)^{1/4}, \tag{6.1}$$

where $G(\theta, \phi)$ is the array gain, $g(\theta, \phi)$ is the element gain, σ is the target Radar Cross Section (RCS), $\mathbf{R}(1,1)$ is the input interference plus noise power and $\mathrm{SINR}_{\mathrm{in}}$ is the minimum input SINR value required for detection. A typical RCS for a small aircraft is 1 m^2 [6]. For this analysis, the input SINR value corresponds to a detection probability of 90 percent when operating in the true forward looking environment, i.e, heterogenous interference and can be found in Fig. 6.9. Table 6.2 gives the theoretical maximum range for JDL, FTS, and SM for a 90 percent detection probability to show the gains obtained using adaptive processing.

The tremendous improvement in maximum range obtained by JDL also shows the potential STAP possesses for the difficult airborne radar target problem. Note the ranges in Table 6.2 are a best case scenario and Skolnik notes the maximum detectable ranges given are not realistic but do provide a measure for comparison [6]. Furthermore, the extension from a linear to a planar array introduces more elements and hence more target samples although transmit gain is held constant. Receive gain is allowed to increase with the increased number of elements. Since $P = 3$ in the scenario under consideration, this increase is a three-fold improvement in coherent integration. This improvement along with the capability to suppress clutter in elevation explains the vastly different maximum detection ranges reflected between the linear and planar arrays shown in Table 6.2.

Conversely, this whole approach could be reversed with a *fixed* detection range and solving for σ to determine an improvement in detectable RCS. This simple analysis would illustrate a forward looking, i.e., fighter, radar's ability to detect stealthy targets.

6.5 Summary

Chapter VI shows the value of elevation adaptivity. Elevation adaptivity is extremely important for forward looking arrays because the range ambiguous clutter increases the clutter rank and 3D STAP is capable of attenuating the range ambiguous clutter. The improvement 3D STAP offers over 2D STAP is shown in the SINR Loss plots and in detection probability plots. The added elevation adaptivity counters the broadened clutter notch and improves slow moving target detection as a result of the narrowed clutter notch. Additionally, the maximum detectable range also increases when using planar arrays.

In fact, radar performance using linear arrays in the forward looking case may not meet desired detection rates as shown through the detection probability analysis comparing 3D and 2D STAP methods. The clutter limited forward looking environment simply requires elevation adaptivity to attenuate the range ambiguous clutter to adequately improve radar performance.

VII. Conclusions

This thesis characterizes the forward looking array radar, models the interference environment, and presents techniques providing suppression of undesirable interference returns to improve target detection. The adaptive interference suppression problem is complicated by the airborne platform motion induced Doppler changing the frequency of the clutter returns. Chapter II gives an overview of the available literature for sidelooking array radars and uses the background for introducing the reader to Space-Time Adaptive Processing (STAP). The sidelooking radar data model is based on the physical model introduced by Ward [2] with extension to planar arrays by Hale [3] and added decorrelation effects by Klemm [1] and Jaffer [4]. Different STAP techniques used to adaptively suppress interference returns are also discussed in Chapter II. The background on sidelooking arrays is very important because the concepts used are extended here to forward looking arrays.

7.1 Forward Looking Data Model

The forward looking array data model is developed using two methods in Chapter III. For the first method, the velocity vector points along the array boresight and simulates a forward looking model. Adding a 90° crab angle to the sidelooking array data model also models the forward looking radar. These two methods produce equivalent models as shown in Section 3.3. Additionally, Chapter IV presents similarities and differences between the forward and sidelooking array data models. The areas of comparison are differences in homogeneity, decorrelation effects, clutter ridges, clutter covariance matrix rank and clutter notches.

7.2 STAP Applied to Linear Forward Looking Arrays

STAP algorithms improve the output Signal-to-Interference-plus-Noise Ratio (SINR) curves over the Signal Match (SM) output SINR curve by placing nulls along the clutter ridge. The reason that raising output SINR is a goal for STAP is because raising output SINR increases target detection probability [5]. Three performance metrics are introduced in Chapter V: output SINR, antenna beam pattern, and detection probability. The antenna beam pattern can show where the STAP algorithm is placing nulls and if the algorithm is nulling the clutter ridge and/or the barrage noise jammer. Unfortunately, STAP for linear arrays is incapable of nulling range ambiguous clutter and even the Matched Filter (MF) is incapable of reaching the Noise limited curve. STAP algorithms do significantly increase detection probability rates over SM with the exception of Factored Time-Space (FTS). However, slow moving target detection is decreased by the wide clutter null so Wang, Bao, and Peng suggest using multiple Pulse Repetition Frequencies (PRF) to get better performance results in STAP for forward looking radar results [28]. Changing the PRF means that the target may change locations with regards to the clutter ridge in the Doppler space. If the target is no longer obscured by the clutter in the Doppler bin, then target detection is improved. However, if the PRF is decreased too much, then Doppler ambiguities occur instead of the range ambiguities. Doppler ambiguities are particularly to be avoided though in the forward looking array case and so the array is extended to give elevation adaptivity to improve results in Chapter VI.

7.3 STAP Applied to Planar Forward Looking Arrays

The STAP algorithms for planar arrays have elevation and azimuth adaptivity so the range ambiguous clutter is capable of being nulled. As a result, the output SINR curves improve dramatically over the SINR curves obtained for linear arrays in Chapter V. However, by adding elevation adaptivity, the number of Degrees of Freedom (DOF) has changed. Therefore, a new performance metric is introduced in Chapter VI: SINR Loss. SINR Loss measures how close the STAP algorithm is to the optimum SINR value regardless of the number of DOF.

As a result, three-dimensional (3D) STAP successfully adaptively suppresses the forward looking radar interference returns, increases target detection and extends the maximum detection range. Detection probability rates significantly increase for 3D STAP over two-dimensional (2D) STAP. Specifically, 3D STAP techniques with adaptivity in elevation, azimuth, and Doppler achieve detection probability improvements of over 10 dB in required input SINR compared to 2D STAP processing. Additionally, 3D STAP improves detection probability versus input SINR rates over 30 dB compared to 2D conventional processing techniques.

As a result, forward looking radars using 3D STAP have the capability to detect targets that conventional processing might miss.

7.4 Contributions

This thesis makes several important contributions in the adaptive interference literature base. First, this research develops the forward looking radar data model with the velocity vector along the array boresight and shows mathematical equivalence to adding a 90° crab angle to the sidelooking radar data model. Additionally, this study fills a void in the literature base for adaptive interference suppression because most adaptive interference suppression research focuses on the sidelooking case.

Next, this thesis illustrates the severe, heterogeneous interference environment for the forward looking case. As a result, sample support is *not* Independently Identically Distributed (iid) and this heterogeneous loss is shown using detection probability curves for linear and planar arrays. Due to the reduced sample support available from the range heterogeneities, parametric estimation theory is used for linear arrays to achieve interference suppression in the forward looking case while using much less sample support than other STAP algorithms. Also due to the range heterogeneities and different clutter shape in the forward looking case, forward looking radar detection probability results degrade compared to the approximately iid sidelooking case.

Finally, this research illustrates the need for elevation adaptivity in the forward looking case so range ambiguous clutter can be mitigated.

7.5 Future Work

Most of the STAP algorithms used in this thesis are based on obtaining the Maximum Likelihood (ML) estimate of the covariance matrix. Since the estimated covariance matrix has to be inverted, the required sample support is two times the number of DOF. The required sample support may not be available in all scenarios, especially in the forward looking array case with increased range heterogeneities. For this reason, parametric estimation theory has been applied to linear arrays to achieve interference suppression with reduced sample support. As discussed in Chapter V, this technique is called the Parametric Adaptive Matched Filter (PAMF) [14, 18]. Future work should extend the PAMF to include elevation adaptivity to be capable of suppressing the range ambiguous clutter in the forward looking array case.

Appendix A. Levinson-Wiggins-Robinson Recursion Estimation Algorithm

The Parametric Adaptive Matched Filter (PAMF) uses an Auto-Regressive (AR) algorithm to estimate the filter coefficients used to whiten the receive signal. The AR estimation algorithm used in this thesis is the Levinson-Wiggins-Robinson Recursion Estimation Algorithm with model order 2 [19].

For the first step, the data vector $\boldsymbol{\chi}$ [2] is reshaped into a matrix with dimensions $N \times M$ for every range cell and denoted $\mathbf{X}$. The forward and backward error covariance matrices, $\mathbf{P}_0^f$ and $\mathbf{P}_0^b$, respectively, are initialized to $\mathbf{R}_{\mathbf{XX}}(0) = \varepsilon\left[\mathbf{X}\mathbf{X}^H\right]$ resulting in $N \times N$ dimensionality where ε represents the expectation operator [20].

The initial forward prediction error filter estimate is

$$\mathbf{A}_1^H(1) = -\boldsymbol{\Delta}_1^H(\mathbf{P}_0^b)^{-1}, \tag{1.1}$$

where $\boldsymbol{\Delta}_p$ is the cross correlation between the forward and backward error residuals at filter p. This cross correlation for filter 1 is $\boldsymbol{\Delta}_1 = \mathbf{R}_{\mathbf{XX}}(1)$, the autocorrelation of $\mathbf{X}$ with a lag of 1. Similarly, the initial backward prediction error filter estimate is

$$\mathbf{B}_1^H(1) = -\boldsymbol{\Delta}_1(\mathbf{P}_0^f)^{-1}. \tag{1.2}$$

Upon a cross correlation update,

$$\boldsymbol{\Delta}_2 = \mathbf{R}_{\mathbf{XX}}(-2) + \mathbf{B}_1^H(1)\mathbf{R}_{\mathbf{XX}}(-1). \tag{1.3}$$

The forward and backward error covariance matrices then become

$$\begin{aligned} \mathbf{P}_1^f &= [\mathbf{I}_N - \mathbf{A}_1^H(1)\mathbf{B}_1^H(1)]\mathbf{P}_0^f \\ \mathbf{P}_1^b &= [\mathbf{I}_N - \mathbf{B}_1^H(1)\mathbf{A}_1^H(1)]\mathbf{P}_0^b. \end{aligned} \tag{1.4}$$

The forward reflection coefficient matrix is defined as

$$\mathbf{\Gamma}_2^f = -\mathbf{\Delta}_2^H (\mathbf{P}_1^b)^{-1}. \tag{1.5}$$

The estimated forward prediction error filter then becomes [19]

$$\begin{aligned} \mathbf{A}_2^H(1) &= \mathbf{A}_1^H(1) + \mathbf{\Gamma}_2^f \mathbf{B}_1^H(1) \\ \mathbf{A}_2^H(2) &= \mathbf{\Gamma}_2^f. \end{aligned} \tag{1.6}$$

These two expressions serve as the foundation for determining the weight vector in Eqn. (2.34).

Bibliography

1. R. Klemm, *Principles of Adaptive Space-Time Processing.* London: IEE, 2002.
2. J. Ward, “Space-time adaptive processing for airborne radar,” Contract F19628-95-C-0002, Lincoln Laboratory, Massachusetts Institute of Technology, Lexington, Massachusetts, December 1994.
3. T. B. Hale, *Airborne Radar Interference Suppression Using Adaptive Three-Dimensional Techniques.* PhD thesis, Air Force Institute of Technology, May 2002.
4. A. Jaffer, M. Baker, W. Ballance, and J. Staub, “Adaptive space-time processing techniques for airborne radars,” Contract F30602-89-D-0028, Hughes Aircraft Company, Fullerton, CA 92634, July 1991.
5. L. Brennan and I. Reed, “Theory of adaptive radar,” *IEEE Transactions on Aerospace and Electronic Systems*, vol. AES-9, No. 2, pp. 237–252, March 1973.
6. M. I. Skolnik, *Introduction to Radar Systems, Second Edition.* New York: McGraw-Hill, Inc., 1980.
7. L. L. Scharf, *Statistical Signal Processing: Detection, Estimation, and Time Series Analysis.* Reading, Massachusetts: Addison Wesley, 1991.
8. G. W. Stimson, *Introduction to Airborne Radar.* Mendham, NJ: SciTech Publishing, Inc., second ed., 1998.
9. A. Graham, *Kronecker Products and Matrix Calculus with Applications.* Ellis Horwood: Mathematics and its Applications, Market Cross House, Cooper Street, Chichester, West Sussex, PO19 1EB, England: Ellis Horwood Limited, 1981.
10. T. B. Hale, “Class notes.” EENG678 Advanced Interference Suppression, June 2003.
11. K. S. Shanmugan and A. M. Breipohl, *Random Signals: Detection, Estimation, and Data Analysis.* New York: Wiley, 1988.
12. L. S. Brooks and I. S. Reed, “Equivalence of the likelihood ratio processor, the maximum signal-to-noise ratio filter, and the wiener filter,” *IEEE Transactions on Aerospace and Electronic Systems*, pp. 690–692, September 1972. Correspondence.
13. H. Wang and L. Cai, “On adaptive spatial-temporal processing for airborne surveillance radar systems,” *IEEE Transactions on Aerospace and Electronic Systems*, vol. 30, pp. 660–669, July 1994.

14. J. R. Roman, M. Rangaswamy, D. W. Davis, Q. Zhang, B. Himed, and J. H. Michels, "Parametric adaptive matched filter for airborne radar applications," *IEEE Transactions on Aerospace and Electronic Systems*, vol. 36, No. 2, pp. 677–692, April 2000.

15. I. S. Reed, J. Mallett, and L. Brennan, "Rapid convergence rate in adaptive arrays," *IEEE Transactions on Aerospace and Electronic Systems*, vol. AES-10, No. 6, pp. 853–863, November 1974.

16. D. M. Boronson, "Sample size considerations in adaptive arrays," *IEEE Transactions on Aerospace and Electronic Systems*, vol. 16, No. 4, pp. 446–451, July 1980.

17. T. B. Hale, M. A. Temple, M. C. Wicks, J. F. Raquet, and M. E. Oxley, "Localized three-dimensional adaptive spatial-temporal processing for airborne radar," in *Proceedings of the 2002 IEE International Radar Conference*, (Edinburgh, United Kingdom), October 2002. Submitted for publication December 2001.

18. J. H. Michels, J. R. Roman, and B. Himed, "Beam control using the parametric adaptive matched filter stap approach," in *Proceedings of the 2003 IEEE National Radar Conference*, May 2003.

19. J. H. Michels, "Multichannel detection using the discrete-time model-based innovations approach," Technical Report RL-TR-91-269, Rome Laboratory, Rome, New York, August 1991.

20. S. L. Marple, *Digital Spectral Analysis with Applications.* Englewood Cliffs, New Jersey: Prentice-Hall, 1987.

21. S. Haykin, *Communication Systems, Fourth Edition.* New York: Wiley, 2001.

22. T. B. Hale, M. A. Temple, and B. L. Crossley, "Ambiguity analysis for pulse compression radar using gold code sequences," in *Proceedings of the 2001 IEEE National Radar Conference*, (Atlanta, GA), May 2001.

23. P. G. Richardson, "Space-time adaptive processing for manoeuvring airborne radar," *IEE Transactions on Electronics and Communication*, vol. 11, No. 1, pp. 57–63, February 1999.

24. L. Brennan and F. Staudaher, "Subclutter visibility demonstration," Technical Report RL-TR-92-21, Adaptive Sensors Incorporated, March 1992.

25. J. T. Caldwell and T. B. Hale, "Space-time adaptive processing for forward looking arrays," in *Accepted to 2004 IEEE National Radar Conference*, April 2004.

26. S. K. Mitra, *Digital Signal Processing: A Computer-Based Approach.* Boston, Massachusetts: McGraw-Hill, 2001.

27. J. T. Caldwell and T. B. Hale, “Parametric adaptive matched filter applied to forward looking radar,” in *Submitted to 2004 SEE International Radar Conference*, October 2004.

28. Y. L. Wang, Y. N. Peng, and Z. Bao, “Space-time adaptive processing for airborne radar with various array orientations,” *IEEE Transactions on Radar, Sonar, and Navigation*, vol. 144, No. 6, pp. 660–669, December 1997.

Index

The index is conceptual and does not designate every occurrence of a keyword.

REPORT DOCUMENTATION PAGE	*Form Approved* *OMB No. 074-0188*

1. REPORT DATE *(DD-MM-YYYY)* 23-03-2004	**2. REPORT TYPE** **Master's Thesis**	**3. DATES COVERED** *(From – To)* Jun 2003 – Mar 2004

4. TITLE AND SUBTITLE FORWARD LOOKING RADAR: INTERFERENCE MODELLING, CHARACTERIZATION, AND SUPPRESSION	**5a. CONTRACT NUMBER**
	5b. GRANT NUMBER
	5c. PROGRAM ELEMENT NUMBER
6. AUTHOR(S) Caldwell, James T., Second Lieutenant, USAF	**5d. PROJECT NUMBER**
	5e. TASK NUMBER
	5f. WORK UNIT NUMBER

7. PERFORMING ORGANIZATION NAMES(S) AND ADDRESS(S) Air Force Institute of Technology Graduate School of Engineering and Management (AFIT/EN) 2950 Hobson Way, Building 640 WPAFB OH 45433-7765	**8. PERFORMING ORGANIZATION REPORT NUMBER** AFIT/GE/ENG/04-02
9. SPONSORING/MONITORING AGENCY NAME(S) AND ADDRESS(ES) AFRL/SNR Attn: Dr. Atindra K. Mitra 2241 Avionics Circle, Bldg. 620 (937) 785-6427 WPAFB OH 45433-7512 e-mail: Atindra.Mitra@wpafb.af.mil	**10. SPONSOR/MONITOR'S ACRONYM(S)**
	11. SPONSOR/MONITOR'S REPORT NUMBER(S)

12. DISTRIBUTION/AVAILABILITY STATEMENT

APPROVED FOR PUBLIC RELEASE; DISTRIBUTION UNLIMITED.

13. SUPPLEMENTARY NOTES

14. ABSTRACT

This research characterizes forward looking radar performance while noting differences with traditionally examined sidelooking radar. The target detection problem for forward looking radar is extremely difficult due to the severe, heterogeneous and range dependent ground clutter. Consequently, forward looking radar detection represents an important but overlooked topic because of the increased difficulty compared to sidelooking radar. This void must be filled since most fighter aircraft use forward looking radar, making this topic intensely interesting to the Air Force.

After characterizing forward looking radar performance, basic radar concepts along with advanced adaptive interference suppression techniques improve the output Signal-to-Interference-plus-Noise Ratio (SINR) and target detection rates using fixed false alarm for linear arrays. However, target detection probabilities and output SINR do not improve enough. Although the methods considered are adaptive in azimuth and Doppler, effective range ambiguous clutter mitigation requires elevation adaptivity, a feature not offered by linear arrays.

The research continues by examining planar arrays. Elevation adaptivity combined with azimuth and Doppler adaptivity allows suppressing range ambiguous clutter and significantly increasing output SINR, detection probability, and maximum detection range. Specifically, three-dimensional Space-Time Adaptive Processing (3D STAP) techniques with adaptivity in elevation, azimuth, and Doppler achieve detection probability improvements of over 10 dB in required input SINR compared to two-dimensional (2D) STAP processing. Additionally, 3D STAP improves detection probability versus input SINR curves over 30 dB when compared to 2D conventional processing techniques.

As a result, forward looking radars using 3D STAP have the capacity to detect targets that conventional processing might miss.

15. SUBJECT TERMS

Radar, Radar Interference, Radar Clutter, Adaptive Filters

16. SECURITY CLASSIFICATION OF:			**17. LIMITATION OF ABSTRACT**	**18. NUMBER OF PAGES**	**19a. NAME OF RESPONSIBLE PERSON** Todd B. Hale, Maj, USAF (ENG)
a. REPORT	**b. ABSTRACT**	**c. THIS PAGE**			**19b. TELEPHONE NUMBER** *(Include area code)* (937) 255-6565, ext 4639; e-mail: Todd.Hale@afit.edu
U	U	U	UU	112	

Standard Form 298 (Rev. 8-98)
Prescribed by ANSI Std. Z39-18